PHYSICAL REVIEW D VOLUME 51, NUMBER 6 15 MARCH 1995

ARTICLES

Spherical resonant-mass gravitational wave detectors

Carl Z. Zhou and Peter F. Michelson
Physics Department, Stanford University, Stanford, California 94305
(Received 16 June 1994)

A spherical gravitational wave antenna is a very promising detector for gravitational wave astronomy because it has a large cross section, isotropic sky coverage, and can provide the capability of determining the wave direction. In this paper we discuss several aspects of spherical detectors, including the eigenfunctions and eigenfrequencies of the normal modes of an elastic sphere, the energy cross section, and the response functions that are used to obtain the noise-free solution to the inverse problem. Using the maximum likelihood estimation method the inverse problem in the presence of noise is solved. We also determine the false-alarm probability and the detection probability for a network of spherical detectors and estimate the detectable event rates for supernova collapses and binary coalescences.

PACS number(s): 04.80.Nn, 95.55.Ym

I. INTRODUCTION

Gravitational wave astronomy has two broad scientific goals: (1) to verify directly the existence of gravitational radiation and (2) to use gravitational radiation as a tool for astronomical observation. The first goal requires detectors of high sensitivity, while the second goal imposes the additional requirement that detectors have good direction resolution and a broad bandwidth.

A spherical detector is a very promising detector for gravitational wave astronomy because it has the following features [1–3]: (1) a relatively large energy cross section, (2) isotropic sky coverage, and (3) direction sensitivity.

As early as 1971 Forward [1] proposed using a spherical antenna to detect gravitational waves. He claimed that by suitably positioning a set of transducers on the sphere, one could determine the direction, the polarization, and the amplitude of a gravitational wave. Later Wagoner and Paik [2] calculated the cross section of a homogeneous elastic sphere and showed that a spherical antenna has a much larger energy cross section than a cylindrical antenna. Recently Johnson and Merkowitz [3] proposed a method of positioning six radial transducers on a truncated icosahedron to construct a nearly spherical detector. They showed that a spherical detector cooled to ultralow temperature can have sensitivity comparable to or even better than the first generation Laser Interferometric Gravitational Wave Observatory (LIGO) detectors in the frequency range around 1 kHz.

Like a spherical detector, a network of six cylindrical detectors with appropriate orientations can also cover the whole sky isotropically and have source direction resolution [4,5]. Such a network with six colocated cylindrical detectors has sensitivity $\frac{1}{7}$ that of a single spherical detector made of the same material and with the same resonant frequency [5].

The ability of a spherical detector to determine the wave direction is very desirable for gravitational wave astronomy. Ideally, gravitational wave observatories should be able to determine both the source direction and the wave forms of gravitational radiation signals. Laser interferometric detectors due to their inherently broad frequency bandwidth will be superior in determining the wave forms. A spherical detector is very promising for estimating the wave direction because it has five degenerate modes interacting with the gravitational wave.

The direction resolution of a spherical detector also helps discriminate against false signals in coincidence experiments. In addition to the requirement that the output of all detectors in a coincidence experiment exceed an energy threshold within a narrow time window, an additional requirement can be imposed on a network of spherical detectors, namely that the detectors provide consistent estimated wave directions. This additional requirement raises the confidence level for detection or, for a given confidence level, it allows the use of a lower-energy threshold for detection and therefore higher sensitivity.

Determination of the direction, the polarization, and the amplitude of a gravitational wave signal is often called the "inverse problem." Dhurandhar and Tinto [6,7] have provided solutions to the inverse problem for detector networks in the noise-free case. Gürsel and Tinto [8] have solved the inverse problem in the presence of noise for a three-interferometer detector network by using time delays between the detectors.

In this paper, we address some issues associated with solving the inverse problem for spherical detectors. The paper is organized as follows. In Sec. II we discuss the normal modes and the energy cross section of a sphere. We show that a spherical detector with an uncoupled transducer configuration is equivalent to five independent single-channel detectors. In Sec. III we discuss the response functions of the five detection channels of

a spherical detector and obtain the noise-free solution to the inverse problem by using these response functions. In Sec. IV we solve the inverse problem in the presence of noise. An algorithm for determining the wave direction with colocated detectors is developed using the maximum likelihood estimation method. The estimation errors are determined both by numerical simulations and analytically in the limit of a high signal-to-noise ratio. We also show that a spherical detector has reasonable direction resolution ($\Delta\Omega \approx 0.3$ sr) even at a relatively low signal-to-noise ratio (average amplitude S/N per channel ≈ 1.4). In Sec. V we discuss coincidence experiments with spherical detectors. The false-alarm probability and the detection probability for a network of spherical detectors are discussed and the event rates for detectable gravity wave signals from supernovae and binary coalescences are estimated for a network of four spherical detectors.

II. INTERACTION OF GRAVITATIONAL RADIATION WITH A SPHERICAL ANTENNA

A. Normal modes of a sphere

1. Toroidal modes and spheroidal modes

A free-vibrating sphere has two classes of normal modes [9]. The first class is the toroidal modes, for which there are no volume changes and no radial displacements. The eigenfunctions of the toroidal modes are of the form [9]

$$\Psi_{lm}^{(t)} = C\psi_l(\kappa r)(\mathbf{r} \times \nabla Y_{lm}) \ , \tag{2.1}$$

where C is the normalized amplitude and Y_{lm} are spherical harmonics. $\kappa^2 = \rho\omega_l^2/\mu$, where ρ is the density of the sphere and μ is the shear modulus. $\psi_l(x)$ is a function given by

$$\psi_l(x) = \left(\frac{1}{x}\frac{d}{dx}\right)^l \left(\frac{\sin x}{x}\right) \ . \tag{2.2}$$

The second class of normal modes is sometimes referred to as the spheroidal modes. These modes can be expressed as [2]

$$\Psi_{lm}^{(s)} = [a_l(r)\hat{\mathbf{e}}_r + b_l(r)R\nabla]Y_{lm}(\theta,\varphi) \ , \tag{2.3}$$

where R is the radius of the sphere, and $a_l(r)$ and $b_l(r)$ are dimensionless radial eigenfunctions determined by the boundary conditions. For a more detailed discussion of $a_l(r)$ and $b_l(r)$, see Wagoner and Paik [2].

In general the spheroidal modes consist of both transverse and radial components. When $l = 0$, there are only radial vibrations, while for $l = 2$ the sphere is distorted into an ellipsoid of revolution becoming alternately prolate and oblate depending on the phase of motion.

2. Interaction with gravitational waves

The response of a normal-mode n to a gravitational wave is governed by the equation [10]

$$\ddot{A}_n + \tau_n^{-1}\dot{A}_n + \omega_n^2 A_n = R_n(t) \ , \tag{2.4}$$

where A_n is the mode amplitude and τ_n is the decay time. $R_n(t)$ is the driving force per unit mass given by [10]

$$R_n(t) = -M^{-1}R_{i0j0}(t)\int \Psi_n^{i^*} x^j \rho \, d^3x \ , \tag{2.5}$$

where M is the mass of the antenna and R_{i0j0} are the components of the Riemann tensor $(i,j = x,y,z)$. The coordinate origin is taken to be the center of mass.

According to general relativity, a gravitational radiation field is a tensor field of massless spin-2 particles. In the wave-based coordinate system, the nonvanishing components of the Riemann tensor are [11]

$$\begin{aligned} R_{x0x0} &= -R_{y0y0} = -\frac{1}{2}\frac{\partial^2}{\partial t^2}h_+ \ , \\ R_{x0y0} &= R_{y0x0} = -\frac{1}{2}\frac{\partial^2}{\partial t^2}h_\times \ , \end{aligned} \tag{2.6}$$

where h_+ and $h_\times$ are the gravitational wave amplitudes of the two independent polarization states.

Appendix A shows that gravitational waves have no effect on the toroidal modes with even l. For spheroidal modes, it has been shown that only the quadrupole modes interact with a tensor gravitational field [2,12]. Before discussing the driving forces for the spheroidal quadrupole modes, it is convenient to introduce real spherical harmonics. The real quadrupole spherical harmonics are defined as

$$\begin{aligned} Y_0 &\equiv Y_{20} \ , \\ Y_{1c} &\equiv \frac{1}{\sqrt{2}}(Y_{2-1} - Y_{2+1}) \ , \\ Y_{1s} &\equiv \frac{i}{\sqrt{2}}(Y_{2-1} + Y_{2+1}) \ , \\ Y_{2c} &\equiv \frac{1}{\sqrt{2}}(Y_{2-2} + Y_{2+2}) \ , \\ Y_{2s} &\equiv \frac{i}{\sqrt{2}}(Y_{2-2} - Y_{2+2}) \ . \end{aligned} \tag{2.7}$$

Like the spherical harmonics $Y_{lm}(\theta,\varphi)$, the real spherical harmonics are orthonormal:

$$\int Y_j(\theta,\varphi)Y_{j'}(\theta,\varphi)d\Omega = \delta_{jj'} \ , \tag{2.8}$$

where the subscript $j = (0, 1c, 1s, 2c, 2s)$.

We can express the eigenfunctions of the fivefold degenerate quadrupole modes in terms of the real spherical harmonics as

$$\Psi_n = [a(r)\hat{\mathbf{e}}_r + b(r)R\nabla]Y_n(\theta,\varphi) \ . \tag{2.9}$$

Here we have dropped the subscript 2 in $a(r)$ and $b(r)$, and the subscript n denotes the modes $(0, 1c, 1s, 2c, 2s)$.

The quadrupole mode driving forces for gravitational waves in the wave-based frame have been given by Wagoner and Paik [2] in terms of spherical harmonics. We

recast their results in terms of real spherical harmonics. In the wave-based coordinate system where the gravitational wave propagates in the z direction, the driving forces are

$$R^{(2c)}(t) = \ddot{h}_+(t)\left(\frac{4\pi}{15}\right)^{1/2}\frac{1}{M}\int [a(r)r + 3b(r)R]\rho r^2 dr \ ,$$
$$R^{(2s)}(t) = -\ddot{h}_\times(t)\left(\frac{4\pi}{15}\right)^{1/2}\frac{1}{M} \times \int [a(r)r + 3b(r)R]\rho r^2 dr \ , \quad (2.10)$$
$$R^{(1c)} = R^{(1s)} = R^{(0)} = 0 \ .$$

A gravitational wave can, in principle, excite all five quadrupole modes. Information about the direction, the amplitude, and the polarization of the wave can be obtained from the response amplitudes of the five quadrupole modes. We will discuss the response functions in Sec. III and solve the inverse problem in the presence of noise in Sec. IV.

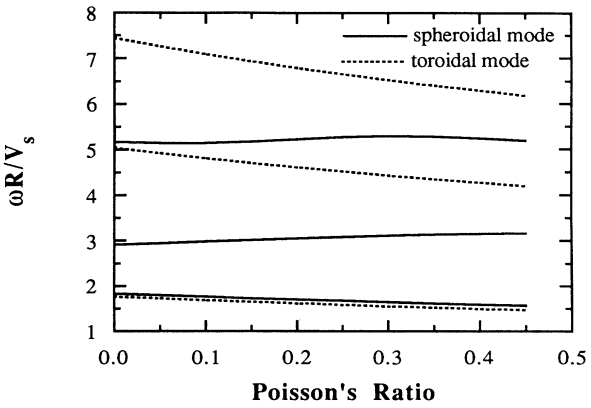

FIG. 1. Normal-mode frequencies of the three lowest spheroidal and toroidal quadrupole modes of an elastic sphere as functions of Poisson's ratio. V_S is the sound velocity of the material and R is the radius of the sphere.

3. *Normal-mode frequencies*

The normal-mode frequencies are important parameters in detector design. Both the toroidal mode and the spheroidal mode frequencies of a free-vibrating sphere can be determined numerically. The toroidal mode frequency is determined by the equation [9]

$$(l-1)\psi_l(\kappa R) + \kappa R\psi_l'(\kappa R) = 0 \ , \quad (2.11)$$

where ψ_l is as defined in Eq. (2.2), and $\kappa^2 = \rho\omega_l^2/\mu$. The spheroidal mode frequency is given by [9]

$$u_l z_l - v_l w_l = 0 \ , \quad (2.12)$$

where

$$u_l = \frac{1}{(2l+1)h^2}\{\kappa^2 R^2\psi_l(hR) + 2(l-1)\psi_{l-1}(hR)\} \ ,$$
$$v_l = -\frac{1}{(2l+1)}\left\{\frac{\kappa^2}{h^2}\psi_l(hR) + \frac{2(l+2)}{hR}\psi_l'(hR)\right\} \ , \quad (2.13)$$
$$w_l = \kappa^2 R^2\psi_l(\kappa R) + 2(l-1)\psi_{l-1}(\kappa R) \ ,$$
$$z_l = \kappa^2\frac{l}{l+1}\left\{\psi_l(\kappa R) + \frac{2(l+2)}{\kappa R}\psi_l'(\kappa R)\right\} \ ,$$

with $h^2 = \omega^2\rho/(\lambda + 2\mu)$.

The quantity $\omega R/V_s$ can be evaluated numerically. V_s is the sound velocity. The results are shown in Fig. 1 for the three lowest spheroidal and toroidal quadrupole modes. The frequencies of the quadrupole modes depend on Poisson's ratio. The toroidal mode frequencies decrease as Poisson's ratio increases, while the spheroidal mode frequencies vary only slightly with Poisson's ratio.

The resonant frequency of a quadrupole mode can be easily obtained from Fig. 1. For example, for an aluminum sphere with a diameter of 3.2 m, the lowest spheroidal quadrupole mode frequency is about 840 Hz, the second lowest frequency is about 1.6 kHz, and the third lowest frequency is about 2.8 kHz.

The lowest toroidal quadrupole mode frequency is about 10% lower than the lowest spheroidal mode frequency. We can distinguish the toroidal modes from the spheroidal modes by using the fact that toroidal modes have no radial displacements.

For a spheroidal detector, the closeness of the toroidal mode and the spheroidal mode frequencies can be used to discriminate among nongravity wave signals. It has been suggested [13,14] that non-Gaussian disturbances such as cosmic rays in a cylindrical detector can be vetoed by comparing the excitation of the second harmonic longitudinal mode of the cylinder with that of the fundamental mode. The second harmonic mode cannot be excited by a gravitational wave. The same veto technique can be used in spheroidal detectors by simultaneously monitoring the excitations of toroidal and spheroidal quadrupole modes, since the toroidal quadrupole modes cannot be excited by a gravitational wave (see Appendix A). The veto should be more efficient than that used in cylindrical detectors because of the closeness of the frequencies of the spheroidal and the toroidal modes.

B. Energy cross section

Wagoner and Paik [2] have compared the cross sections of a cylinder, a circular disk, and a sphere, and shown that a sphere has the largest energy cross section. This makes a sphere a very natural shape for resonant-mass gravity wave detectors.

In general, a resonant-mass detector has an energy absorption cross section [10]

$$\Sigma = \frac{1}{2\pi}\int \sigma(\omega)d\omega = \frac{\pi}{4}\frac{G}{c^3}\frac{|(I_{jk} - \delta_{jk}I_{ll}/3)e^{jk}|^2}{M}\omega_0^2 \ , \quad (2.14)$$

where ω_0 is the resonant frequency of the detector, e^{jk} is the component of the wave polarization tensor, and

$$I_{jk} = \int \rho(\Psi_j x_k + \Psi_k x_j) d^3x$$

is the moment-of-inertia factor.

Let d be the wavelength of a normal mode with a resonant frequency f_0 such that $d = V_s/f_0$. The energy cross section in terms of d can be rewritten as

$$\Sigma = \frac{\pi}{4}\frac{G}{c^3}\frac{\omega_0^2 \rho^2 d^8}{M}\left|\frac{(I_{jk} - \delta_{jk} I_{ll}/3)e^{jk}}{\rho d^4}\right|^2$$

$$= \frac{G}{c^3}\frac{\rho V_S^5}{f_0^3}\Pi\,, \tag{2.15}$$

where

$$\Pi = \frac{\pi^3 \rho d^3}{M}\left|\frac{(I_{jk} - \delta_{jk} I_{ll}/3)e^{jk}}{\rho d^4}\right|^2 . \tag{2.16}$$

Π is a dimensionless quantity that mainly depends on the geometric shape of the detector. It is a useful quantity for evaluating detectors with different geometric shapes. Π is referred to as the reduced energy cross section.

The energy cross section is proportional to the quantity $\rho V_S^5/f_0^3$. The cross section can therefore be improved by using high-density, high-sound-velocity materials [15].

The energy cross section of a spherical detector is given by [2]

$$\Sigma = \frac{4\pi}{5}\frac{G}{c^3}\frac{\rho\omega^2}{R}\left\{\int\left[a(r)\frac{r}{R} + 3b(r)\right] r^2 dr\right\}^2 . \tag{2.17}$$

The reduced cross sections Π of a spherical antenna and of a cylindrical detector are easily calculated numerically. In Fig. 2 these cross sections are compared. The reduced cross section of a cylindrical antenna depends on the ratio of diameter and length D/L. The higher this ratio, the larger the energy cross section. For the cylindrical antenna, we assumed the parameters of the Stanford cryogenic 4K antenna [16] in our calculation.

A spherical antenna is sensitive to sources over the whole sky because of its spherical symmetry. For the same reason, the energy cross section of a sphere is also independent of the direction and the polarization of the incoming wave. By contrast, a cylindrical antenna has only partial sky coverage and the average cross section is $\frac{4}{15}$ that of the antenna in the optimal orientation. Figure 2 shows both the optimal cross section and the average cross section of a cylindrical detector.

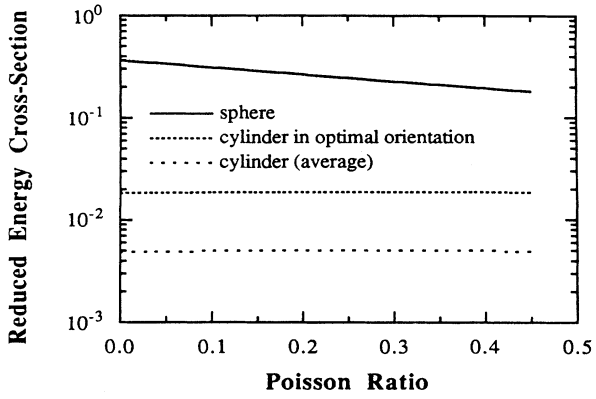

FIG. 2. Comparison of the reduced cross section of a sphere and a cylinder. The diameter-length ratio of the cylinder is 0.27. The average cross section of the cylinder is $\frac{4}{15}$ that of an optimally oriented cylinder and is obtained by averaging over the wave direction and polarization.

From Fig. 2, we see that the reduced cross section of a sphere is a function of Poisson's ratio, decreasing as Poisson's ratio increases, while the reduced cross section of a cylinder only slightly depends on Poisson's ratio. For aluminum antennas with Poisson's ratio of 0.35, the reduced cross section of a sphere is about 10 times larger than the optimal cross section of a cylinder and about 40 times larger than the average cross section of a cylinder. Johnson and Merkowitz [3] found that the energy cross section of a sphere is about 56 times larger than the average cross section of a cylinder. The difference between their result and ours comes from the fact that we have used a different diameter-length ratio for a cylinder in the calculation.

Table I lists the parameters of a spherical detector and a cylindrical detector with identical materials and resonant frequencies. The mass of the spherical antenna is about 10 times that of the cylindrical antenna. Obviously the increased mass is the main reason for the spherical detector having a larger cross section than a cylindrical antenna.

TABLE I. Parameters of an aluminum cylindrical antenna and a spherical antenna.

Spherical antenna	Cylindrical antenna
$f = 840$ Hz	$f = 840$ Hz
$D = 3.2$ m	$L = 3.1$ m, $D = 0.84$ m
$M = 4.6 \times 10^4$ kg	$M = 4.8 \times 10^3$ kg
$\Sigma = \frac{1}{2\pi}\int \sigma(\omega)d\omega = 8.7 \times 10^{-20}$ cm^2 Hz	$\Sigma = 1\ ver 2\pi \int \sigma(\omega)d\omega = 7.6 \times 10^{-21}$ cm^2 Hz
(independent of orientation)	(for the optimal orientation)

C. Antenna readout

1. *Uncoupled transducer configuration*

A transducer is a device that converts the mechanical vibrations of the antenna into electrical signals. Most of the transducers currently used on resonant-mass detectors incorporate mechanical resonators, which are used to optimize the signal-to-noise ratio of the detector [17–21].

Since a spherical antenna has five degenerate quadrupole modes interacting with gravitational waves in the frequency range of interest, at least five transducers need to be mounted on the surface of the sphere to monitor the dynamical strains of the five modes. The arrangement of these transducers is an important detector design consideration. Proper placement of the transducers optimizes the performance of the detector and makes the signal analysis straightforward, in principle.

Johnson and Merkowitz [3] have proposed mounting six transducers on the surface of a nearly spherical truncated icosahedron to observe the five nearly degenerate quadrupole modes. The six transducers are sensitive to radial displacements of the antenna. Through a linear transformation, the six transducers yield five independent "mode channels," which are the readouts of the five quadrupole modes.

Here we propose a different transducer arrangement in which only five transducers are required and each one is coupled to one and only one of the five degenerate quadrupole modes. Each transducer and the associated quadrupole mode form a detection channel, and all five channels are independent of each other.

In order to find such an uncoupled transducer configuration, it is necessary to find a position for each transducer that is a node of all the modes but one. The nodes on the surface of a sphere depend not only on the location but also on the direction in which the transducer is sensitive to motion. As mentioned before, most transducers currently used on resonant-mass detectors are themselves mechanical resonators. Typically these devices are sensitive to motion in only one direction. For the other directions the effects of a transducer are mainly to introduce small frequency shifts due to the relatively small transducer mass attached to the much larger mass of the antenna. These are higher-order effects which we will not discuss here.

In order to find the nodes of the quadrupole modes, we examine the angular dependence of the eigenfunctions (shown in Table II). At the north pole there is no radial motion of the quadrupole modes except for the ψ_0 mode. Accordingly, a transducer sensitive to radial displacements ("radial transducer") can be placed at the north pole to couple to the ψ_0 mode. On the equator, only the ψ_{1c} and the ψ_{1s} modes have nonzero motions in the θ direction and only the ψ_{2c} and the ψ_{2s} modes have nonvanishing motions in the φ direction. The ψ_{1c} and the ψ_{1s} modes are 90° orthogonal to each other, and the ψ_{2c} and the ψ_{2s} modes are 45° orthogonal to each other. Therefore, we can position four "tangential" transducers on the equator, two in the θ direction to monitor the ψ_{1c} and the ψ_{1s} modes, respectively, and the other two in the φ direction to monitor the ψ_{2c} and the ψ_{2s} modes, respectively. This ideal uncoupled transducer configuration is summarized in Table III.

TABLE II. Angular dependence of the quadrupole modes.

Mode	r direction	θ direction	φ direction
ψ_0	$3\cos^2\theta - 1$	$\sin 2\theta$	0
ψ_{1c}	$\cos\theta \sin\theta \cos\varphi$	$\cos 2\theta \cos\varphi$	$\cos\theta \sin\varphi$
ψ_{1s}	$\cos\theta \sin\theta \sin\varphi$	$\cos 2\theta \sin\varphi$	$\cos\theta \cos\varphi$
ψ_{2c}	$\sin^2\theta \cos 2\varphi$	$\sin 2\theta \cos 2\varphi$	$\sin\theta \sin 2\varphi$
ψ_{2s}	$\sin^2\theta \sin 2\varphi$	$\sin 2\theta \sin 2\varphi$	$\sin\theta \cos 2\varphi$

TABLE III. Uncoupled transducer configuration.

Mode	Location (θ, φ)	Direction
ψ_0	(0,0)	r
ψ_{1c}	$\left(\frac{\pi}{2}, 0\right)$	θ
ψ_{1s}	$\left(\frac{\pi}{2}, \frac{\pi}{2}\right)$	θ
ψ_{2c}	$\left(\frac{\pi}{2}, \frac{\pi}{4}\right)$	φ
ψ_{2s}	$\left(\frac{\pi}{2}, \pi\right)$	φ

Since each transducer is coupled to only one mode, the back action noise from the transducer and its preamplifier will affect that mode only and the thermal noise of the particular quadrupole mode will only appear at the output of the corresponding transducer. Therefore, a quadrupole mode and its associated transducer and amplifier form an independent detection channel. The five quadrupole modes along with the five uncorrelated transducers then effectively act as five independent detectors with different orientations. By using the uncoupled transducer configuration, the detector noise analysis becomes very simple, and the analysis techniques developed for cylindrical antennas can be directly applied to spherical antennas. Of course in a real detector the situation will, in practice, be more complicated in that there will likely be some coupling between the readout channels. Taking account of such coupling only complicates the analysis but will not change the conclusions regarding signal-to-noise ratio, direction sensitivity, etc.

2. *Effective mass*

In optimizing the transducer design, particularly the choice of masses for the transducer mechanical resonators, the effective mass of the antenna [18,21] is an important parameter. The effective mass is defined as [19]

$$E_k = \tfrac{1}{2} M_{\text{eff}} V_l^2 \ , \tag{2.18}$$

where E_k is the kinetic energy of the mode of interest, and V_l is the amplitude of the velocity component in the direction of interest $\hat{\mathbf{e}}_l$. The effective mass depends on both location and direction. The larger the effective mass, the smaller the velocity amplitude. At a node, the effective mass becomes infinitely large.

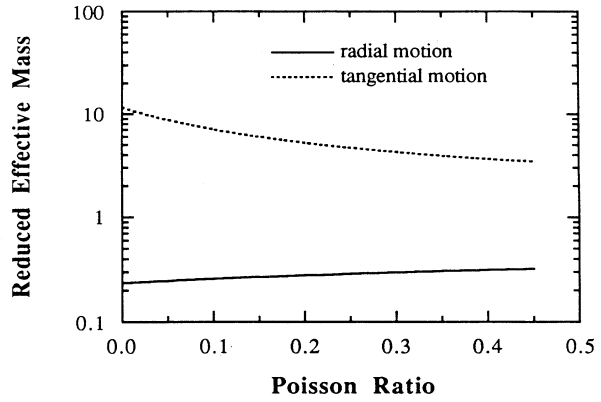

FIG. 3. Reduced effective masses of a spherical antenna. The solid line is the reduced effective mass of the antenna appropriate for a transducer mounted on the north pole of the sphere and sensitive to radial motion. The dashed line is the reduced antenna effective mass for a transducer mounted on the equator of the sphere that senses tangential motion.

The effective mass of a node is calculated using the corresponding eigenfunction. If a normal-mode n is excited with amplitude A_n, the kinetic energy of the mode is

$$E_k = \tfrac{1}{2}\int \rho \Psi_n^2 \dot{A}_n^2 \, d^3x = \tfrac{1}{2} M \dot{A}_n^2 \ . \tag{2.19}$$

The velocity in direction $\hat{\mathbf{e}}_l$ at any point on the surface is $V_l = (\Psi_n \cdot \hat{\mathbf{e}}_l)\dot{A}_n$. Hence the effective mass is

$$M_{\rm eff} = \frac{2M}{(\Psi_n \cdot \hat{\mathbf{e}}_l)^2} \ . \tag{2.20}$$

We define $M_{\rm eff}/M$ as the reduced effective mass and calculate the effective masses versus Poisson's ratio (shown in Fig. 3) for the uncoupled transducer configuration discussed above. The antenna effective mass for the radial transducer, which is coupled to the ψ_0 mode, is about one-third the physical mass of the sphere. The effective masses for the four tangential transducers are identical, about four times the physical mass of the sphere for Poisson's ratio of 0.3.

Because the antenna effective masses for all the tangential transducers are identical, four identical detection channels can be formed by attaching four identical transducers appropriately to the sphere. By properly scaling the masses of the transducer resonators, the radial and the tangential transducer channels can be made identical, i.e., have the same frequency response function. The five detection channels in the uncoupled transducer arrangement can therefore be considered identical except for orientation.

III. THE DETECTION RESPONSE FUNCTION

A. Introduction

The response of a detector to a gravitational wave depends on the signal frequency spectrum, the antenna energy cross section, the frequency response functions of the transducer and the amplifier, and the detector orientation relative to the incoming wave. The energy cross section and the normal-mode driving forces of a spherical antenna have been reviewed in the preceding section. The frequency response characteristics of the transducers and the amplifiers typically used in cylindrical resonant-mass detectors have been derived elsewhere [20,22], and the results can be used here. Thus, we only need to consider the effects of orientation on the response of a spherical detector in this section.

As mentioned in Sec. II, the energy cross section of a spherical detector is independent of the direction and the polarization of the incoming wave. However, each of the five independent detection channels responds differently to a gravitational wave depending on the direction and the polarization of the wave. It is the orientation dependence of the channel response that allows a solution to the inverse problem with a single spherical antenna.

In this section we begin with a review of the response function of a single channel detector and then use these results to study the response of a spherical detector. Finally we give the noise-free solution to the inverse problem in terms of the channel response functions. The effects of noise are introduced in Sec. IV.

B. The response function of a single-channel detector

The orientation dependence of the response function of a single-channel detector is usually characterized by the wave tensor and the detector tensor [7,8,23–26]. A plane gravitational wave with amplitudes $h_+(t)$ and $h_\times(t)$ associated with the two independent polarization states can be described by a symmetric and trace-free (STF) tensor as

$$h_{ij}(t) = h_+(t)W_{+ij} + h_\times(t)W_{\times ij} \ , \tag{3.1}$$

where W_{+ij} and $W_{\times ij}$ are STF tensors, which depend only on the wave direction angles (θ,φ). The explicit forms of $W_{+ij}(\theta,\varphi)$ and $W_{\times ij}(\theta,\varphi)$ are given in Appendix B.

A detector can also be represented by a symmetric detector tensor D_{ij}, which depends on the orientation and the geometry of the detector. The orientation-dependent part of the detector response function, $R(t)$, is determined by the scalar product of the wave tensor and the detector tensor as

$$\begin{aligned} R(t) &= D_{ij}h^{ij}(t) \\ &= h_+(t)F_+(\theta,\varphi) + h_\times(t)F_\times(\theta,\varphi) \ , \end{aligned} \tag{3.2}$$

where

$$\begin{aligned} F_+(\theta,\varphi) &= D_{ij}W_+^{ij}(\theta,\varphi) \ , \\ F_\times(\theta,\varphi) &= D_{ij}W_\times^{ij}(\theta,\varphi) \ . \end{aligned} \tag{3.3}$$

We refer to $F_+(\theta,\varphi)$ and $F_\times(\theta,\varphi)$ as the orientation fac-

tors.

The detector tensor D_{ij} is determined from Eq. (3.2) by using the wave tensor and the response function. Since the wave tensor is symmetric and trace free, D_{ij} can be represented in either a symmetric or a symmetric and trace-free form. Both forms yield the same results. For example, the detector tensor of a cylindrical antenna whose longitudinal axis is in the direction $\hat{\boldsymbol{l}}$ can be either

$$D_{ij} = \hat{l}_i \hat{l}_j \ , \tag{3.4}$$

or, in the trace-free form,

$$D_{ij} = \hat{l}_i \hat{l}_j - \tfrac{1}{3}\delta_{ij} \ . \tag{3.5}$$

Both forms generate the same response function.

We assume that the detector has a linear frequency response function. The detector can then be considered as a linear filter with a frequency-dependent transfer function $L(\omega)$. The response of a detector to a gravitational wave signal is then

$$\begin{aligned} s(t) &= \frac{1}{2\pi}\int L(\omega)\tilde{R}(\omega)e^{i\omega t}d\omega \\ &= \frac{1}{2\pi}D_{ij}\int L(\omega)\tilde{h}_{ij}(\omega)e^{i\omega t}d\omega \\ &= A(t)F_+(\theta,\varphi) + B(t)F_\times(\theta,\varphi) \ , \end{aligned} \tag{3.6}$$

with

$$\begin{aligned} A(t) &= \frac{1}{2\pi}\int L(\omega)\tilde{h}_+(\omega)e^{i\omega t}d\omega \ , \\ B(t) &= \frac{1}{2\pi}\int L(\omega)\tilde{h}_\times(\omega)e^{i\omega t}d\omega \ , \end{aligned} \tag{3.7}$$

where $\tilde{R}(\omega)$, $\tilde{h}_{ij}(\omega)$, $\tilde{h}_+(\omega)$, and $\tilde{h}_\times(\omega)$ are the Fourier transforms of $R(t)$, $h_{ij}(t)$, $h_+(t)$, and $h_\times(t)$, respectively.

The output of the detector is the sum of the signal and an effective noise $n(t)$:

$$y(t) = s(t) + n(t) \ . \tag{3.8}$$

$n(t)$ includes contributions from noise sources in the antenna, the transducer, and the amplifier.

C. The response functions of a spherical detector

In order to study the response functions of a spherical detector or a detector network, we define a detection channel as a device that generates an output as described by Eq. (3.8) for a gravity wave input signal. A cylindrical detector has a single detection channel. A spherical detector, with either the uncoupled transducer configuration discussed in Sec. III B or the scheme of Johnson and Merkowitz [3], has five independent detection channels associated with the five degenerate quadrupole modes.

The mode driving forces of a gravitational wave in the wave-based frame have been derived by Wagoner and Paik [2]. Only the $2c$ and the $2s$ modes can be excited by the impinging gravity wave with the driving forces given by Eq. (2.10) as

$$\begin{aligned} R^{(2c)}(t) &= R_0 \frac{d^2 h_+(t)}{dt^2} \ , \\ R^{(2s)}(t) &= -R_0 \frac{d^2 h_\times(t)}{dt^2} \ , \end{aligned} \tag{3.9}$$

where the superscripts $(2c)$ and $(2s)$ represent the $2c$ and the $2s$ modes in the wave-based frame and

$$R_0 = \left(\frac{4\pi}{15}\right)^{1/2} \frac{M}{R^2}\int [a(r)r + 3Rb(r)]\rho r^2 \, dr \ . \tag{3.10}$$

The driving force in the laboratory coordinate system can be obtained through a coordinate transformation from the wave-based frame. The driving force at any point $\mathbf{x}$ within a sphere can be expressed in terms of the normal-mode driving forces $R^{(n)}(t)$ as

$$\mathbf{f}(\mathbf{x},t) = \sum_n R^{(n)}(t)\Psi^{(n)}(\mathbf{x},t) \ . \tag{3.11}$$

Since a spherical detector is a relatively narrow bandwidth detector, we consider only the five degenerate quadrupole modes to be within the detector bandwidth. The radial eigenfunctions are coordinate invariant because they are the same for the five degenerate modes. The coordinate transformation only affects the angular eigenfunctions. The transformation of angular eigenfunctions is given by

$$Y^{(n)}(\theta_L,\varphi_L) = T_{n,n'}(\theta,\varphi)Y^{(n')}(\theta_W,\varphi_W) \ , \tag{3.12}$$

where $T_{n,n'}(\theta,\varphi)$ is the transformation matrix, $Y^{(n)}(\theta_L,\varphi_L)$ is the angular eigenfunction of the mode n in the laboratory frame, and $Y^{(n')}(\theta_W,\varphi_W)$ is the angular eigenfunction of the mode n' in the wave-based frame. (θ,φ) are the usual Euler angles, which transform the laboratory frame into the wave-based frame and represent the two wave direction angles. The third Euler angle ψ has been set to zero, since it merely rotates the axes to which the two polarization states are referred and therefore has no effect on the final results.

The transformation matrix for spherical harmonics is a standard result [27]. We derive the transformation matrix $T_{n,n'}$ for real spherical harmonics and show the explicit form of $T_{n,n'}$ in Appendix C.

The transformation matrix has the following important properties: (1) The inverse matrix of $T_{n,m}$ is its transpose $T_{m,n}$, (2) $\sum_n T_{n,m}^2 = \sum_n T_{m,n}^2 = 1$, and (3) $\sum_n T_{n,m}T_{n,p} = \sum_n T_{m,n}T_{p,n} = \delta_{mp}$.

From Eqs. (3.9), (3.11), (3.12) and the properties of the transformation matrix, the mode driving forces in the laboratory frame can be expressed as

$$\begin{aligned} R^{(n)}(t) &= \sum_{n'} T_{n',n}R^{(n')}(t) \\ &= R_0\{T_{2c',n}\ddot{h}_+(t) - T_{2s',n}\ddot{h}_\times(t)\} \ , \end{aligned} \tag{3.13}$$

and the channel output signal in the frequency domain

is

$$\tilde{s}^{(n)}(\omega) = T_{2c',n}(\theta,\varphi)L(\omega)\tilde{h}_+(\omega) - T_{2s',n}(\theta,\varphi)L(\omega)\tilde{h}_\times(\omega) \ , \tag{3.14}$$

where $L(\omega)$ is the channel frequency response function that includes the scaling factor R_0. We have assumed $L(\omega)$ is the same for all channels, i.e., all the channels are identical.

Comparing Eq. (3.14) with Eq. (3.3), we obtain the orientation factors of the five quadrupole modes in the laboratory frame:

$$\begin{aligned} F_{+n}(\theta,\varphi) &= T_{2c,n}(\theta,\varphi) \ , \\ F_{\times n}(\theta,\varphi) &= -T_{2s,n}(\theta,\varphi) \ . \end{aligned} \tag{3.15}$$

These orientation factors for a spherical antenna have the properties

$$\sum_n F^2_{+n}(\theta,\varphi) = \sum_n F^2_{\times n}(\theta,\varphi) = 1 \ , \tag{3.16}$$

and

$$\sum_n F_{+n}(\theta,\varphi)F_{\times n}(\theta,\varphi) = 0 \ . \tag{3.17}$$

The elements of the detector tensors of the five channels are found from Eq. (3.2) by using the orientation factors obtained from Eq. (3.16). The nonzero elements of the detector tensors are

$$\begin{aligned} D^{(0)}_{33} &= -\frac{\sqrt{3}}{2} \ , \\ D^{(1c)}_{23} &= D^{(1c)}_{32} = -\tfrac{1}{2} \ , \\ D^{(1s)}_{13} &= D^{(1s)}_{31} = -\tfrac{1}{2} \ , \\ D^{(2c)}_{11} &= -D^{(2c)}_{22} = \tfrac{1}{2} \ , \\ D^{(2s)}_{12} &= D^{(2s)}_{21} = -\tfrac{1}{2} \ , \end{aligned} \tag{3.18}$$

where the superscripts denote the channels.

D. A solution to the inverse problem in the noise-free case

The inverse problem can be solved by using the response amplitudes of five suitably arranged detection channels. In the following we first present the general solution to the noise-free inverse problem and then apply it to a spherical detector.

Since the wave tensor is symmetric and trace free, we can accordingly describe the wave by a five-element matrix **H**:

$$\mathbf{H} = \begin{pmatrix} \tilde{h}_{11}(\omega) \\ \tilde{h}_{22}(\omega) \\ \tilde{h}_{12}(\omega) \\ \tilde{h}_{13}(\omega) \\ \tilde{h}_{23}(\omega) \end{pmatrix} \ . \tag{3.19}$$

We can also form a five-element matrix **S** from the output signals of the five detection channels:

$$\mathbf{S} = \begin{pmatrix} \tilde{S}^{(1)}(\omega) \\ \tilde{S}^{(2)}(\omega) \\ \tilde{S}^{(3)}(\omega) \\ \tilde{S}^{(4)}(\omega) \\ \tilde{S}^{(5)}(\omega) \end{pmatrix} \ , \tag{3.20}$$

where $\tilde{S}^{(n)}(\omega)$ is the Fourier transform of the nth channel output signal.

If all the five channels have an identical frequency response function $L(\omega)$, then **S** is determined from **H** as

$$\mathbf{S} = \mathbf{L}(\omega)\mathbf{D}\mathbf{H} \ , \tag{3.21}$$

where **D** is a matrix formed from the elements of the detector tensors $D^{(n)}_{ij}$:

$$\mathbf{D} = \begin{pmatrix} D^{(1)}_{11} - D^{(1)}_{33} & D^{(1)}_{22} - D^{(1)}_{33} & D^{(1)}_{12} + D^{(1)}_{21} & D^{(1)}_{13} + D^{(1)}_{31} & D^{(1)}_{23} + D^{(1)}_{32} \\ D^{(2)}_{11} - D^{(2)}_{33} & D^{(2)}_{22} - D^{(2)}_{33} & D^{(2)}_{12} + D^{(2)}_{21} & D^{(2)}_{13} + D^{(2)}_{31} & D^{(2)}_{23} + D^{(2)}_{32} \\ D^{(3)}_{11} - D^{(3)}_{33} & D^{(3)}_{22} - D^{(3)}_{33} & D^{(3)}_{12} + D^{(3)}_{21} & D^{(3)}_{13} + D^{(3)}_{31} & D^{(3)}_{23} + D^{(3)}_{32} \\ D^{(4)}_{11} - D^{(4)}_{33} & D^{(4)}_{22} - D^{(4)}_{33} & D^{(4)}_{12} + D^{(4)}_{21} & D^{(4)}_{13} + D^{(4)}_{31} & D^{(4)}_{23} + D^{(4)}_{32} \\ D^{(5)}_{11} - D^{(5)}_{33} & D^{(5)}_{22} - D^{(5)}_{33} & D^{(5)}_{12} + D^{(5)}_{21} & D^{(5)}_{13} + D^{(5)}_{31} & D^{(5)}_{23} + D^{(5)}_{32} \end{pmatrix} \ , \tag{3.22}$$

where the superscripts denote the channel numbers. If the inverse of **D** exists, **H** is uniquely determined by the five channel response amplitudes as

$$\mathbf{H} = L^{-1}(\omega)\mathbf{D}^{-1}\mathbf{S} \ . \tag{3.23}$$

The requirement that **D** have an inverse matrix can be satisfied by suitable arrangement of the orientations of the five channels. Obviously no two channels should be in the same orientation.

Once **H** is determined, the inverse problem is solved. The wave direction angles are obtained from the wave tensor as [6]

$$\begin{aligned} \tan\varphi &= \frac{h_{22}h_{13} - h_{12}h_{23}}{h_{12}h_{13} - h_{11}h_{23}} \ , \\ \tan\theta &= \frac{-h_{13}}{h_{11}\sin\varphi - h_{12}\cos\varphi} \ . \end{aligned} \tag{3.24}$$

Equation (3.24) is a solution of the inverse problem with five detection channels in the noise-free case. Clearly there is an ambiguity between diametrically opposite points in the sky because both (θ,φ) and $(\pi-\theta,\pi+\varphi)$ satisfy the same equation.

For a spherical antenna, the inverse **D** matrix exists, and the wave tensor can be determined from the response amplitudes of the five independent detection channels as

$$\begin{aligned}
\tilde{h}_{11}(\omega) &= L^{-1}(\omega)\left[\frac{1}{\sqrt{3}}\tilde{s}^{(0)}(\omega)+\tilde{s}^{(2c)}(\omega)\right] ,\\
\tilde{h}_{22}(\omega) &= L^{-1}(\omega)\left[\frac{1}{\sqrt{3}}\tilde{s}^{(0)}(\omega)-\tilde{s}^{(2c)}(\omega)\right] ,\\
\tilde{h}_{12}(\omega) &= -2L^{-1}(\omega)\tilde{s}^{(2s)}(\omega) ,\\
\tilde{h}_{13}(\omega) &= -2L^{-1}(\omega)\tilde{s}^{(1s)}(\omega) ,\\
\tilde{h}_{23}(\omega) &= -2L^{-1}(\omega)\tilde{s}^{(1c)}(\omega) .
\end{aligned} \tag{3.25}$$

The wave direction angles are thus

$$\begin{aligned}
\tan\varphi &= -\frac{\left[\frac{1}{\sqrt{3}}s^{(0)}-s^{(2c)}\right]s^{(1s)}+2s^{(2s)}s^{(1c)}}{\left[\frac{1}{\sqrt{3}}s^{(0)}+s^{(2c)}\right]s^{(1c)}+2s^{(2s)}s^{(1s)}} ,\\
\tan\theta &= \frac{2s^{(1s)}}{\left[\frac{1}{\sqrt{3}}s^{(0)}+s^{(2c)}\right]\sin\varphi+2s^{(2s)}\cos\varphi} .
\end{aligned} \tag{3.26}$$

Equation (3.26) shows that the inverse problem can be solved with the five independent detection channels of a spherical detector.

The number of channels needed to uniquely solve the inverse problem is of interest. The detector response is a function of four variables: two wave direction angles (θ,φ), and the two amplitudes $h_+(t)$ and $h_\times(t)$ associated with the two independent polarization states. At first glance it would appear that with a suitable channel configuration, using the response amplitudes of four detection channels should be sufficient for solving the inverse problem for the four unknowns. However, because the two direction angles appearing in the wave tensor elements are in the forms of trigonometric functions, we cannot construct a set of linear equations with the four channel outputs. Thus the solution of the inverse problem is usually not unique in this case.

Since we have shown that in the noise-free case a suitably arranged five-channel system can uniquely solve the inverse problem, except for the direction ambiguity associated with diametrically opposite points on the sky, we conclude that five channels is the minimum number of channels needed to solve the inverse problem when only the response amplitudes are used.

IV. SOLVING THE INVERSE PROBLEM IN THE PRESENCE OF NOISE

A. The signal-to-noise ratio of a multichannel detection system

In the presence of noise, the inverse problem can only be solved approximately with an estimator. We shall first discuss the signal-to-noise ratio of a multichannel system before discussing the estimation process because it is the figure-of-merit used for evaluating and optimizing a detector system. We will show that the maximum signal-to-noise ratio of a multichannel system is the sum of the maximum signal-to-noise ratio of each individual channel.

Consider a set of data y_i, which is the sum of a known signal s_i and noise n_i:

$$y_i = s_i + n_i, \quad i = 1,2,\ldots,N . \tag{4.1}$$

Assume n_i is uncorrelated, has zero mean, and variance σ_i^2. The maximum signal-to-noise ratio that can be achieved by constructing an optimal filter is (Appendix D)

$$S/N = \sum_{i=1}^{N}\frac{s_i^2}{\sigma_i^2} . \tag{4.2}$$

Now consider an N-channel detection system in which each channel has been noise whitened and appropriately sampled so that the noise is uncorrelated. For simplicity, we also assume the noise is uncorrelated between the channels. In fact, even if the data are correlated, we can always linearly transform them into a set of uncorrelated random variables with zero means if the covariance matrix is positive definite [28]. We assume this is the case for all the detector systems of interest.

Under the assumption of uncorrelated random variables, the N channels generate an $N\times M$ uncorrelated data set if each channel takes M data. Applying Eq. (4.2) to this data set, the maximum signal-to-noise ratio of the multichannel system is

$$S/N = \sum_{i=1}^{N}\sum_{k=1}^{M}\frac{S'^{(i)^2}(t_k)}{\sigma'^{(i)^2}} = \sum_{i=1}^{N}(S/N)^{(i)} , \tag{4.3}$$

where the superscript i indicates the channel number and $(S/N)^{(i)}$ is the maximum signal-to-noise ratio of the ith channel. Thus, the maximum signal-to-noise ratio of a multichannel system is the sum of the maximum signal-to-noise ratio of each channel. For the purpose of evaluating a multichannel detection system, we define the signal-to-noise ratio as the sum of the S/N of each channel.

B. Comparison of S/N between a spherical detector and a cylindrical detector

In order to compare a five-channel spherical detector with a single-channel cylindrical detector, we evaluate their maximum signal-to-noise ratios for the same gravity wave signal. It is appropriate to use the concept of noise temperature to describe the signal-to-noise ratio of a resonant-mass detector when the incoming gravity wave is a short pulse [20,22]. The signal-to-noise ratio of a single-channel detector is then given by

$$S/N = \frac{E}{k_B T_n} , \tag{4.4}$$

where E is the energy the gravitational wave would deposit in an antenna initially at rest, k_B is Boltzmann's constant, and T_n is the detector noise temperature for pulse detection.

A spherical detector with five independent channels is equivalent to five independent single-channel detectors. For purposes of comparison, we assume that each channel of a spherical detector has the same frequency response and the same noise temperature as those of the corresponding cylindrical detector.

The maximum signal-to-noise ratio of a spherical detector is

$$S/N = \sum_n (S/N)^{(n)} = \sum_n \frac{E^{(n)}}{k_B T_n} = \frac{E_s}{k_B T_n} , \quad (4.5)$$

where the summation is over the five channels. $E^{(n)}$ is the signal energy received by the nth channel, E_S is the total energy deposited in the sphere, and T_n is the channel noise temperature. Similarly, the maximum signal-to-noise ratio of a cylindrical antenna is

$$S/N = \frac{E_C}{k_B T_n} , \quad (4.6)$$

where E_C is the total energy deposited in the cylinder.

The difference in the signal-to-noise ratio depends only on the difference in the energy cross section, since we have assumed that both the spherical and cylindrical detectors have the same noise temperature. The spherical detector improves the signal-to-noise ratio by a factor of about 40 (see also Sec. II B).

C. Estimation of the wave direction

Gürsel and Tinto have developed an algorithm for estimating the wave direction by using both the detector response amplitudes and the delay times between the detectors [8]. Since there are no delay times between the five channels of a single spherical detector, the Gürsel-Tinto algorithm is not applicable, and we need to develop an estimation method for a colocated detector network. In the following we first develop the general algorithm for solving the inverse problem with a colocated multichannel system and then apply it to a spherical detector.

To develop such an algorithm we need to select an estimator. There are two considerations when selecting an estimator [29]. First, consider the bias, which is the difference between the estimated value and the true value of the parameter. An ideal estimator is unbiased. Second, an ideal estimator should minimize the variance of the estimator σ_λ^2, given by

$$\sigma_\lambda^2 = E\{(\lambda - E\{\hat{\lambda}\})^2\} , \quad (4.7)$$

where $E\{\cdots\}$ denotes an ensemble average, and λ and $\hat{\lambda}$ are the true value and the estimated value of the parameter, respectively.

There is a minimum variance bound for an unbiased estimator [29]. Although such an ideal estimator does not always exist, if one does exist it will be the maximum likelihood (ML) estimator, and it will be unique [29]. In practice, it is often found that if the signal-to-noise ratio is high, the ML estimator approaches the minimum variance bound. Therefore, we will use the ML estimator to solve the inverse problem in the presence of noise. The least-squares method and the ML method are identical when the noise is Gaussian.

The likelihood function f is the probability density function for having a set of output data for a given set of parameter values [28,29]:

$$f = p(y_1, \ldots, y_N | \lambda_1, \ldots, \lambda_M) , \quad (4.8)$$

where $y_1, \ldots, y_N$ are the output data and $\lambda_1, \ldots, \lambda_M$ are the set of parameters. The ML estimate is the set of parameter values, which maximizes the likelihood function. Sometimes it is more convenient to work with the log likelihood function:

$$L = \ln p(y_1, \ldots, y_N | \lambda_1, \ldots, \lambda_M) . \quad (4.9)$$

Maximizing the likelihood function is equivalent to maximizing the log likelihood function.

Consider N colocated detection channels in coincidence. Assume that each channel has an optimal filter or a nearly optimal filter to maximize the signal-to-noise ratio. The optimal filter is the matched filter if the form of the input signal is known [28]. In practice, this type of filters cannot be constructed because the wave form of gravitational radiation signals cannot be known beforehand. However, a nearly optimal filter for detection of impulsive signals can be found for a resonant-mass detector [22] by assuming that the signal bandwidth is much broader than the detector bandwidth so that the input signal can be approximated by a δ-function-like signal. The nearly optimal filters are identical for identical detectors.

In response to a short impulsive signal input, the nearly optimum filter for each channel will generate one datum whose signal-to-noise ratio has been maximized. The estimation process is relatively simple because only N data need to be processed when there are N detection channels in coincident operation to detect gravitational waves. The data are usually represented as complex numbers that contain information about both the amplitude and the phase of the signal.

For simplicity we assume that all the channels are identical and the noise in each channel is Gaussian and uncorrelated. After being nearly optimally filtered, the N channels generate a set of N data, $y^{(1)}, \ldots, y^{(N)}$, for an impulsive input signal. The likelihood function for having this set of data generated by the wave propagating at direction (θ, φ) with the two polarization state amplitudes $h_+(t)$ and $h_\times(t)$ is

$$\begin{aligned} f &= \prod_{i=1}^{N} p(y^{(i)} | A, B, \theta, \varphi) \\ &= \prod_{i=1}^{N} \frac{1}{2\pi} \exp\left(- \frac{[y^{(i)} - AF_+^{(i)}(\theta,\varphi) - BF_\times^{(i)}(\theta,\varphi)]^2}{2\sigma^2} \right), \end{aligned} \quad (4.10)$$

where A and B, as described in Eq. (3.7), are the channel response amplitudes to the two independent polarization states of the wave, and σ^2 is the noise variance of a channel that has been assumed to be the same for all channels.

To estimate the wave direction, first maximize the log likelihood function with respect to A and B. This gives

$$A = \frac{\left(\sum F_+^{(i)} y^{(i)}\right)\left(\sum F_\times^{(i)2}\right) - \left(\sum F_\times^{(i)} y^{(i)}\right)\left(\sum F_+^{(i)} F_\times^{(i)}\right)}{\left(\sum F_+^{(i)2}\right)\left(\sum F_\times^{(i)2}\right) - \left(\sum F_+^{(i)} F_\times^{(i)}\right)^2} ,$$

$$B = \frac{\left(\sum F_\times^{(i)} y^{(i)}\right)\left(\sum F_+^{(i)2}\right) - \left(\sum F_+^{(i)} y^{(i)}\right)\left(\sum F_+^{(i)} F_\times^{(i)}\right)}{\left(\sum F_+^{(i)2}\right)\left(\sum F_\times^{(i)2}\right) - \left(\sum F_+^{(i)} F_\times^{(i)}\right)^2} . \tag{4.11}$$

Substituting Eq. (4.11) into Eq. (4.10) gives the maximized likelihood function, which is a function of (θ, φ) only. A "likelihood map" is generated by plotting this function in the (θ, φ) plane. The maximum value on the likelihood map corresponds to the estimated wave direction. It is only necessary to plot the likelihood map on half of the (θ, φ) plane because there is an ambiguity between opposite points on the sky as discussed earlier.

We can now apply the maximum likelihood estimation method to a spherical detector. Because the channel orientation factors of a spherical detector are orthonormal [see Eqs. (3.16) and (3.17)], Eq. (4.11) simplifies to

$$A = \sum_n F_+^{(n)} y^{(n)} ,$$

$$B = \sum_n F_\times^{(n)} y^{(n)} , \tag{4.12}$$

where the summations are over the five channels $(0, 1c, 1s, 2c, 2s)$. Equation (4.12) can be substituted into Eq. (4.10), which can then be used to generate a likelihood map given a set of input data $y^{(n)}$. In Fig. 4 some examples of likelihood maps generated by numerical simulations are shown. The simulated signals are given by

$$s^{(n)} = A_0 F_+^{(n)}(\theta_0, \varphi_0) + B_0 F_\times^{(n)}(\theta_0, \varphi_0) , \tag{4.13}$$

where n denotes the channel number, A_0 and B_0 are two complex numbers representing the two response amplitudes, and (θ_0, φ_0) are the direction angles of the simulated wave. A_0 and B_0 are chosen to correspond to a wave of a given energy and polarization state. The signal energy is equal to $A_0^2 + B_0^2$.

Five random complex numbers are assigned to the five channels to simulate the effective noise $n^{(n)}$. Both the real and imaginary parts of the complex numbers are drawn from a Gaussian distribution with variance σ_0^2. The variance of the channel effective noise σ^2 is the sum of the variances of the real and imaginary parts, $\sigma^2 = 2\sigma_0^2$.

The channel outputs are the sum of the signal and the effective noise:

$$y^{(n)} = s^{(n)} + n^{(n)} . \tag{4.14}$$

The energy signal-to-noise ratio for a spherical detector is, from Eq. (4.2),

$$S/N = \frac{A_0^2 + B_0^2}{\sigma^2} . \tag{4.15}$$

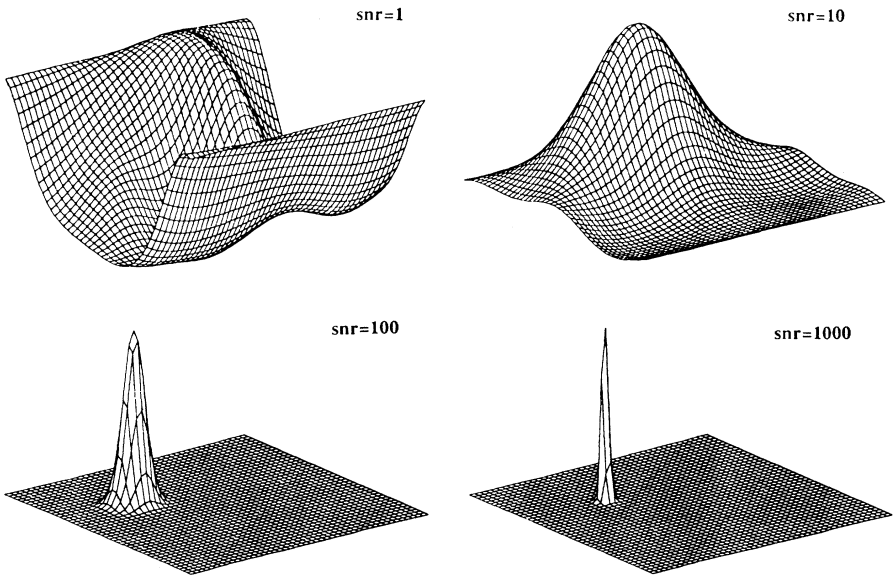

FIG. 4. Examples of likelihood maps for a spherical detector with different signal-to-noise ratios. The maps are for one hemisphere of the sky. The true direction of the source almost coincides with the peak location on the $S/N = 1000$ map.

Substituting the simulated channel outputs into Eqs. (4.12) and (4.10), a likelihood map can be made for a set of output data $y^{(0)},\ldots,y^{(2s)}$. The estimated wave direction is obtained from the location on the map where the likelihood function is maximum.

Figure 4 shows typical likelihood maps for a spherical detector with different signal-to-noise ratios. There is a single peak on each map even for a relatively low signal-to-noise ratio ($S/N = 10$, which corresponds to 1.4 of an average single-channel amplitude S/N), indicating that the solution to the inverse problem is unique. It can also be seen from Fig. 4 that the higher the signal-to-noise ratio, the sharper the peak and the smaller the deviation between the peak location and the true wave direction.

D. Estimation errors

Direction estimation errors for a spherical detector can be evaluated either numerically or analytically. The numerical results are obtained from Monte Carlo simulations and an analytic expression of the estimation errors is obtained in the limit of high signal-to-noise ratio.

1. Monte Carlo simulations

In the Monte Carlo simulations two hundred trials were run for each input signal. For each run the simulated signal and the effective noise were generated according to the method discussed earlier.

Figure 5 is scatter plots showing the estimated wave direction for 200 trials each for various values of the signal-to-noise ratio. The simulated wave signal was a linearly polarized gravitational wave propagating in the direction $\theta_0 = 1$ rad and $\varphi_0 = 2$ rad. The choice of wave direction and polarization was varied and virtually no change in the estimation errors was found.

From Fig. 5 we can see the estimated wave direction varies from trial to trial as expected. When $S/N = 1$, the distribution of points is almost uniform over the sky, indicating that the direction estimation is completely random. As the signal-to-noise ratio increases to about 10, the distribution of trials starts to converge on the vicinity of the true wave direction. From these simulations the minimum energy S/N required for direction estimation is approximately 10 for a spherical detector. As the S/N continues to increase, the distribution of estimated directions becomes narrower.

Two quantities can be used to characterize the direction estimation errors. One is the deviation angle α, which is defined as the angle between the estimated wave direction (θ,φ) and the true wave direction (θ_0,φ_0). α is given by

$$\alpha = \arccos[\sin\theta\,\sin\theta_0\,\cos(\varphi-\varphi_0) + \cos\theta\,\cos\theta_0]\ . \tag{4.16}$$

The other is the estimation error used by Gürsel and Tinto [8],

$$\Delta\Omega = E\{\pi[(\theta-\theta_0)^2 + \sin^2\theta_0(\varphi-\varphi_0)^2]\}\ , \tag{4.17}$$

where $E\{\cdots\}$ denotes the ensemble average.

From the numerical simulations the probability P that an estimated wave direction has a deviation angle larger than α has been computed. Figure 6 shows the probabil-

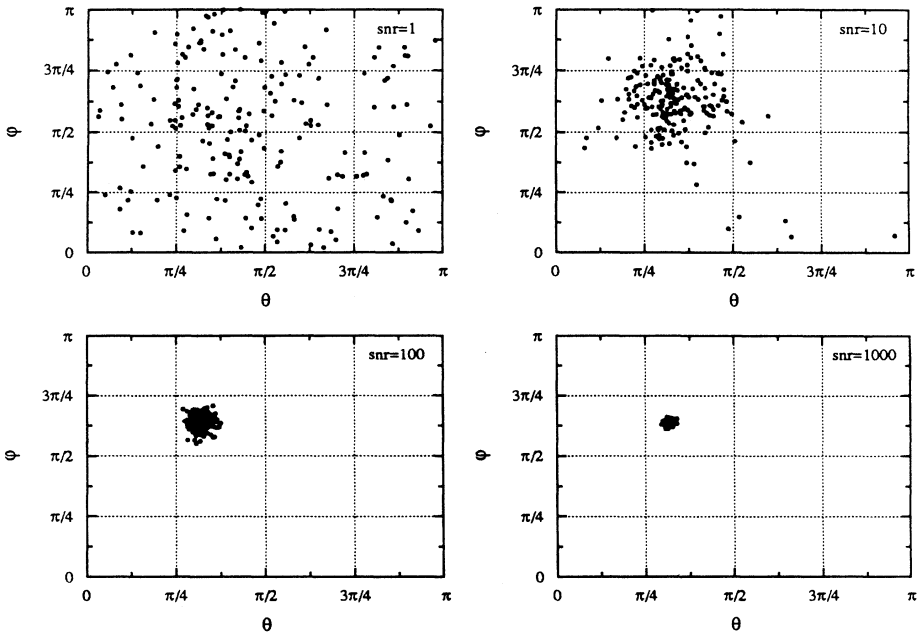

FIG. 5. Source direction estimates for a spherical detector from numerical simulations. The simulated wave is linearly polarized with the direction ($\theta = 1$ rad, $\varphi = 2$ rad). The choices of the wave direction and polarization are arbitrary. Each point is an estimated direction derived from a single numerical simulation trial. Two hundred trials were run for each input signal, i.e., for each S/N.

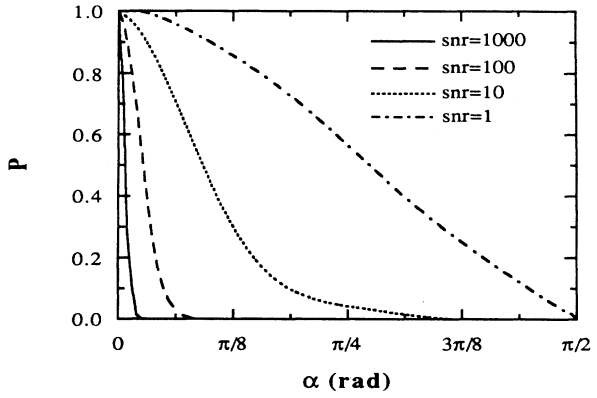

FIG. 6. Probability P that the estimated source direction deviates from the true source direction by an angle larger than α.

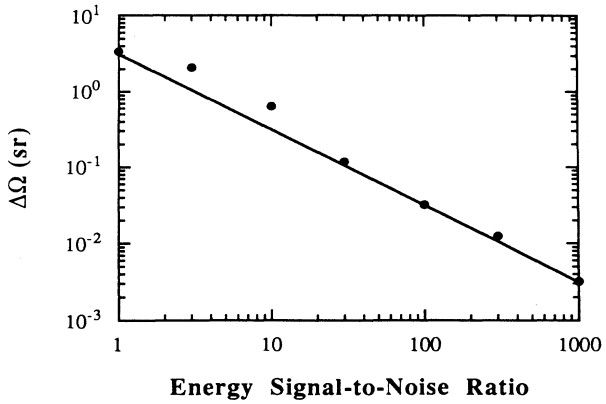

FIG. 7. Direction estimation error $\Delta\Omega$ as a function of the signal-to-noise ratio. The points are derived from numerical simulations and the solid line is an analytic result obtained in the limit of high signal-to-noise ratio.

ity P vs the angle α for different signal-to-noise ratios. For $S/N = 10$, 90% of the trials result in deviation angles less than 0.5 rad. As S/N increases to 1000, this angle decreases to less than 4.7×10^{-2} rad.

In Fig. 7 we show the estimation error $\Delta\Omega$ versus the signal-to-noise ratio. The dots are obtained from the numerical simulations and the solid line is an analytic approximation discussed below.

2. Direction estimation error in the limit of high signal-to-noise ratio

The estimation error can also be derived analytically in the limit of high signal-to-noise ratio. Recall that the likelihood map corresponds to the likelihood function maximized with respect to A and B. The maximized log likelihood function for a spherical detector is

$$L' = \sum_n y^{(n)2} - \left(\sum_n F_+^{(n)}(\theta,\varphi) y^{(n)}\right)^2 - \left(\sum_n F_\times^{(n)}(\theta,\varphi) y^{(n)}\right)^2 . \tag{4.18}$$

The estimated direction is found by maximizing the log likelihood function L' with respect to (θ,φ). This generates two equations:

$$\begin{aligned}\frac{\partial L'}{\partial\theta} &= \frac{\partial}{\partial\theta}\left(\sum F_+^{(n)} y^{(n)}\right)\left(\sum F_+^{(n)} y^{(n)*}\right) + \left(\sum F_+^{(n)} y^{(n)}\right)\frac{\partial}{\partial\theta}\left(\sum F_+^{(n)} y^{(n)*}\right) \\ &\quad + \frac{\partial}{\partial\theta}\left(\sum F_\times^{(n)} y^{(n)}\right)\left(\sum F_\times^{(n)} y^{(n)*}\right) + \left(\sum F_\times^{(n)} y^{(n)}\right)\frac{\partial}{\partial\theta}\left(\sum F_\times^{(n)} y^{(n)*}\right) \\ &= 0 , \\ \frac{\partial L'}{\partial\varphi} &= \frac{\partial}{\partial\varphi}\left(\sum F_+^{(n)} y^{(n)}\right)\left(\sum F_+^{(n)} y^{(n)*}\right) + \left(\sum F_+^{(n)} y^{(n)}\right)\frac{\partial}{\partial\varphi}\left(\sum F_+^{(n)} y^{(n)*}\right) \\ &\quad + \frac{\partial}{\partial\varphi}\left(\sum F_\times^{(n)} y^{(n)}\right)\left(\sum F_\times^{(n)} y^{(n)*}\right) + \left(\sum F_\times^{(n)} y^{(n)}\right)\frac{\partial}{\partial\varphi}\left(\sum F_\times^{(n)} y^{(n)*}\right) \\ &= 0 .\end{aligned} \tag{4.19}$$

An expansion of Eq. (4.19) to first order in $(\theta - \theta_0)$ and $(\varphi - \varphi_0)$, where (θ_0, φ_0) is the true wave direction, gives the estimated wave direction as

$$\begin{aligned}\theta &= \theta_0 + \Delta\theta , \\ \varphi &= \varphi_0 + \Delta\varphi\end{aligned} \tag{4.20}$$

with

$$\Delta\theta = \frac{\sum(A_0^*(\partial F_+^{(n)}/\partial\theta) + B_0^*(\partial F_\times^{(n)}/\partial\theta))n^{(n)} + \sum(A_0(\partial F_+^{(n)}/\partial\theta) + B_0(\partial F_\times^{(n)}/\partial\theta))n^{(n)*}}{2(A_0^2 + B_0^2)} , \tag{4.21}$$

$$\Delta\varphi = \frac{\sum(A_0^*(\partial F_+^{(n)}/\partial\varphi) + B_0^*(\partial F_\times^{(n)}/\partial\theta) + 2\cos\theta_0 A_0^* F_\times^{(n)} - 2\cos\theta_0 B_0^* F_+^{(n)})n^{(n)}}{2\sin^2\theta_0(A_0^2 + B_0^2)}$$
$$+ \frac{\sum(A_0(\partial F_\times^{(n)}/\partial\varphi) + B_0(\partial F_\times^{(n)}/\partial\theta) + 2\cos\theta_0 A_0 F_\times^{(n)} - 2\cos\theta_0 B_0 F_+^{(n)})n^{(n)*}}{2\sin^2\theta_0(A_0^2 + B_0^2)} .$$

Two important conclusions follow from Eq. (4.21). (1) The direction estimator is unbiased:

$$E\{\Delta\theta\} = 0 , \qquad E\{\Delta\varphi\} = 0 . \tag{4.22}$$

(2) $\Delta\theta$ and $\Delta\varphi$ are Gaussian with variances,

$$\sigma_\theta^2 = E\{(\Delta\theta)^2\} = \frac{\sigma^2}{2(A_0^2 + B_0^2)} = \frac{1}{2(S/N)} , \tag{4.23}$$

$$\sigma_\varphi^2 = E\{(\Delta\varphi)^2\} = \frac{\sigma^2}{2\sin^2\theta_0(A_0^2 + B_0^2)} = \frac{1}{2\sin^2\theta_0(S/N)} ,$$

where $S/N = (A_0^2 + B_0^2)/\sigma^2$ is the energy signal-to-noise ratio.

The direction estimation error is obtained from Eq. (4.23) as

$$\begin{aligned}\Delta\Omega &= E\{\pi[(\Delta\theta)^2\sin^2\theta_0(\Delta\varphi)^2]\} \\ &= \pi[\sigma_\theta^2 + \sin^2\theta_0\sigma_\varphi^2] \\ &= \frac{\pi}{S/N} .\end{aligned} \tag{4.24}$$

In Fig. 7, this analytic result for the direction estimation error (solid line) is compared with the numerical results. The numerical and analytic results are in good agreement at high signal-to-noise ratio ($S/N > 30$). At lower signal-to-noise ratio the estimation errors from the numerical simulation are higher than those obtained with the analytic result. When the signal-to-noise ratio is close to 1, the estimation error saturates. This is because at very low signal-to-noise ratio the estimation error approaches the upper limit obtained when the estimated directions are uniformly scattered over the sky. As noted above, the signal-to-noise ratio needs to be higher than ~ 10 in order to obtain a reasonable estimate of the wave direction.

Note that the energy signal-to-noise ratio of a multichannel system is different from the amplitude signal-to-noise ratio of a single-channel detector. A five-channel system with an energy $S/N = 10$ corresponds to an amplitude signal-to-noise ratio of 1.4 per channel on average. Thus, with a spherical detector and a relatively low amplitude signal-to-noise ratio per channel, a reasonable estimate of the wave direction can be obtained.

E. Comparison of a spherical detector with a network of laser interferometric detectors

Long-base-line laser interferometric detectors are projected to have a high sensitivity to gravitational waves [30]. A network of three such detectors can provide information about the wave direction [8]. Here we compare the direction resolution of a spherical detector with that of a network of interferometric detectors.

1. A network of three interferometric detectors

Gürsel and Tinto have developed an algorithm to solve the inverse problem for a network of interferometers using the delay times between the detectors [8]. They also did numerical simulations of a three-interferometer network. Because Gürsel and Tinto used a slightly different definition of signal-to-noise ratio than we have used and because their simulations were done for a specific gravity wave signal, we first review their definition of signal-to-noise ratio and then apply their simulated signal to a spherical detector in order to compare the two types of detectors.

The Gürsel-Tinto expression for the signal-to-noise ratio is [6]

$$\left(\frac{S}{N}\right)' = \frac{A'}{\sqrt{S_h f_{\max}}} , \tag{4.25}$$

where S_h is the noise spectral density of the detector, $f_{\max} = 40$ kHz is the detector bandwidth, and A' is the amplitude of the signal received by the detector. When the detector is in the optimal orientation, the amplitude of the received signal is equal to that of the incoming wave, $A' = A$. In their simulation Gürsel and Tinto also include bandpass linear filters so that the amplitude signal-to-noise ratio for each detector becomes

$$\left[\frac{S}{N}\right]_{\rm alt} = \frac{A'}{\sqrt{S_h \Delta f_{\rm bandpass}}} \approx \sqrt{20}\left(\frac{S}{N}\right)' , \tag{4.26}$$

where $\Delta f_{\rm bandpass} = 2$ kHz is the frequency bandwidth of the bandpass filter used in the simulations. Now consider a simple numerical example to compare the different signal-to-noise ratio expressions. When $(S/N)' = 10$ for a detector with the bandpass filter, the actual am-

plitude signal-to-noise ratio is $[S/N]_{\rm alt} \approx 45$ and $S/N = 3[S/N]^2_{\rm alt} = 6000$ for a network of three detectors, where S/N is the multichannel signal-to-noise ratio defined in Sec. IV A.

The signal in Gürsel and Tinto's simulations was a one-cycle, circularly polarized sinusoid: $h_+(t) = A\sqrt{2}\cos(\omega t)$ and $h_\times(t) = A\sqrt{2}\sin(\omega t)$, $0 \le \omega t \le 2\pi$. The amplitude A was varied, depending on the signal-to-noise ratio, while the frequency $\omega/2\pi$ was allowed to vary randomly in the range 770–2000 Hz.

The three laser interferometers were assumed identical, one located in southern Germany and one each on the east and west coast of the U.S.A. Gürsel and Tinto performed simulations for various source locations because the three-interferometer network does not have isotropic sensitivity. The source locations were chosen to lie on a grid defined by the angles (θ, φ) with $0 \le \theta \le \pi$ and $0 \le \varphi \le 2\pi$. The grid steps were $\pi/10$ in the angle θ and $\pi/20$ in the angle φ, resulting in 400 points on the celestial sphere.

Gürsel and Tinto used the least-squares method to estimate source direction. The least-squares method is equivalent to the ML estimation method in the case of Gaussian noise [29]. Unlike the maximum likelihood estimate for a spherical detector, which typically has a single peak on the likelihood map even at low signal-to-noise ratio, the least-squares estimate in the Gürsel-Tinto simulation was found to have a large number of local minima in the presence of noise, implying that the estimate cannot always converge to the correct source location when the signal-to-noise ratio is low. Thus, in order to have source direction resolution, Gürsel and Tinto concluded that a minimum $(S/N)' \ge 2.1$ is required for each detector. This value is large compared to that for a spherical detector. If each detector has a $(S/N)'$ of 2.1 then the multichannel S/N is 265 for this three-interferometer network, while the minimum S/N required for a spherical detector to have direction resolution is about 10.

Gürsel and Tinto [8] have performed simulations for two cases: (1) detectors with nearly optimal filters and (2) detectors without nearly optimal filters. The nearly optimal filters are constructed by setting a threshold value in the frequency domain. The amplitude of the signal Fourier transform is set to zero if it is smaller than the threshold value, and is left unchanged if it is larger. Gürsel and Tinto have estimated the direction estimation errors both analytically and numerically. The analytic results are obtained by assuming that the least-squares function can be well approximated by a quadratic form in the neighborhood of the minimum. The numerical results are obtained by numerical simulations in which the simulated signal is applied to each grid point on the celestial sphere. The Gaussian white noise in each detector is then simulated by a normally distributed deviate with zero mean and unit variance and the least-squares method is used to estimate the source locations. For each source location the simulation is performed only once and the estimation error is obtained from the difference between the estimated and the true source locations.

The direction resolution depends on the source location, since the sensitivities of the interferometer network are source direction dependent. Gürsel and Tinto have estimated the direction estimation errors both analytically and numerically for each source grid point on the celestial sphere. Table IV summarizes their results for the case of $S/N = 10$ (see Figs. 20 and 23 of Ref. [8]). The analytical and numerical results are not in good agreement, especially in the case without the nearly optimal filters. This is probably because the numerical simulation has been performed only once for each source location, and thus the numerical results reflect the statistical fluctuations.

2. *The sensitivity of a 50-mK spherical detector*

For comparison, we apply the signal used in the Gürsel-Tinto simulation to a spherical detector. The total energy deposited on the detector is [10]

$$E_s = \frac{\pi}{4}\frac{c^3}{G} f_0^2 [\tilde{h}_+^2(f_0) + \tilde{h}_\times^2(f_0)]\Sigma \ , \tag{4.27}$$

where f_0 is the resonant frequency of the spherical antenna, $\tilde{h}_+(f_0)$ and $\tilde{h}_\times(f_0)$ are the Fourier transforms of $h_+(t)$ and $h_\times(t)$ evaluated at the resonant frequency of the detector, and Σ is the integrated energy cross section. For a 3.2-m-diam aluminum sphere, $\Sigma = 8.7\times10^{-20}$ cm^2 Hz.

The Fourier transforms of the one-cycle, circularly polarized sinusoid are

$$|\tilde{h}_+(f_0)| = |\tilde{h}_\times(f_0)| = \frac{1}{\sqrt{2}}\frac{A}{f_0} \ . \tag{4.28}$$

TABLE IV. Distribution of estimation errors in the Gürsel-Tinto simulations.

	Number of points							
	With nearly optimal filter				Without nearly optimal filter			
$\Delta\Omega$ (sr)	Analytic method		Numerical method		Analytic method		Numerical method	
No resolution	183	(45.8%)	183	(45.8%)	58	(14.5%)	58	(14.5%)
$\ge 10^{-3}$	0	(0%)	32	(8.0%)	45	(11.3%)	61	(15.3%)
10^{-3}–10^{-4}	76	(19.0%)	49	(12.2%)	260	(65.0%)	70	(17.5%)
10^{-4}–10^{-5}	121	(30.2%)	46	(11.5%)	37	(9.2%)	86	(21.5%)
$< 10^{-5}$	20	(5.0%)	90	(22.5%)	0	(0%)	125	(31.2%)

Thus, the total energy deposited in the detector is

$$E_s = \frac{\pi}{4}\frac{c^3}{G}A^2\Sigma = 2.77\times10^{19}\ \mathrm{A}^2\ \mathrm{ergs}\ . \quad (4.29)$$

In the lossless limit [21], the noise of a resonant-mass detector is dominated by the noise from the mechanical amplifier which consists of a transducer and a preamplifier. For an inductive transducer with a superconducting quantum interference device (SQUID) preamplifier, the noise temperature of the detector in this limit is [16]

$$T_n = \left(\frac{2T}{k_B}\frac{S_\epsilon\omega_0}{Q_e}\right)^{1/2}\ , \quad (4.30)$$

where T is the physical temperature of the antenna, Q_e is the electrical Q of the mechanical amplifier, and S_ϵ is the SQUID input energy sensitivity. The Stanford 4-K detector [13] operated near the lossless limit with $Q_e = 3\times10^4$, $T = 4.2$ K, and $S_\epsilon = 10^5\hbar$, resulting in $T_n = 3$ mK. The Stanford 50-mK cylindrical detector [16], which is now under construction, is expected to have $T_n = 1$ μK, or a noise energy of $20\hbar$, with $Q_e = 10^6$ and $S_\epsilon = 20\hbar$.

Since most of the techniques developed for the readout of a cylindrical detector can be directly applied to a spherical detector, the noise energy of a large spherical antenna operating at 50-mK temperature is expected to be about $20\hbar$ using current technology.

3. Comparison of a spherical detector with an interferometer detector network

We now compare a 50-mK spherical detector operating with $T_n \sim 1$ μK with a network of interferometers operating at the sensitivity level estimated for the initial LIGO because both detector designs are based on present state-of-the-art technology. We assume the same type of signal as used in the Gürsel-Tinto simulations. The signal frequency is centered around 1 kHz. We compare two quantities: (1) the minimum signal energy required for a detector system to have direction resolution and (2) the direction estimation error.

The expected sensitivity of the initial LIGO interferometers is about 1×10^{-22} $\mathrm{Hz}^{-1/2}$ at 1 kHz, and the expected sensitivity of the advanced LIGO detectors is about 1×10^{-23} $\mathrm{Hz}^{-1/2}$ in the same frequency region [30]. As discussed before, the minimum $(S/N)'$ for a three-interferometer network to have a useful direction resolution is 2.1 for each detector. This requirement is equivalent to an average $(S/N)' = 2.1$, or $(S/N)' = 3.56$ for a detector in the optimal orientation. Substituting the projected sensitivity of the initial LIGO detector into Eq. (4.25) and letting $(S/N)' = 3.56$, we obtain the minimum signal amplitude required for direction resolution as $A = 7.6\times10^{-20}$.

On the other hand, the minimum multichannel S/N for a spherical detector to have useful direction resolution is 10. Assuming $T_n = 1$ μK for a spherical detector, from Eqs. (4.29) and (4.5) the minimum wave amplitude is $A = 6.3\times10^{-21}$. Thus, a spherical detector is superior to the interferometer network in estimating the source direction for signals with relatively small amplitudes.

Now compare the direction estimation error for the two detector systems with the same input signal. Consider the signal used in the Gürsel-Tinto simulation. When $(S/N)' = 10$ for an interferometric detector, the signal amplitude $A = 2.1\times10^{-19}$ for an initial LIGO detector in the optimal orientation. With the same signal impinging on a 50-mK spherical detector, the direction estimation error is $\Delta\Omega = 2.9\times10^{-4}$ sr, independent of the source location, while the direction estimation error of the interferometric detector network depends on the source direction (see Table IV). The analytic results (Table IV) show that, for the network of interferometric detectors with the nearly optimal filters, 35% of points on the sky have direction resolution better than that of the spherical detector, and for the network of interferometric detectors without the nearly optimal filters, only 9% of points have direction resolution better than that of a spherical detector.

The above comparison is done with the signal frequency centered at about 1 kHz. The sensitivity of interferometric detectors is expected to improve as the signal frequency decreases [30], but such improvements do not improve the direction resolution very much because the direction estimation error is inversely proportional to the square of the frequency as estimated with a geometric approximation [8]:

$$\Delta\Omega = \frac{2c^2}{\pi^2 S_0\cos\psi\, f_0^2 (S/N)^2_{\mathrm{alt}}}\ , \quad (4.31)$$

where S_0 is the area of the triangle defined by the locations of the three detectors, and ψ is the angle between the source direction and the normal to the plane of the three detectors.

A spherical detector complements the capabilities of an interferometer network. At low frequencies ($\sim$ 200 Hz) interferometers will likely have higher sensitivity, while at higher frequencies ($\sim$ 1 kHz) a spherical detector can have better performance [3]. Interferometers, because of their intrinsic broad-band sensitivity, are superior in extracting information about the time-dependent waveform, whereas a spherical detector can provide all-sky coverage and, under certain circumstances, provide a superior estimate of the source direction.

F. Signal parameter estimation for the known direction case

1. The ML estimator

Signal parameter estimation when the source direction is known is potentially of importance because in some circumstances a suspected gravitational wave source may be identified by optical or other astronomical observations, or the source location may be determined approximately with a spherical detector, and the detailed wave form needs to be estimated with two or more interferometric detectors. In these situations estimates of the amplitude

and polarization of the wave are required.

The inverse problem becomes much simpler in the known direction case. Analytic solutions can be obtained in the case of identical detection channels with independent Gaussian noise sources. These solutions can provide conditions for optimizing the relative orientations of the detectors in a network.

The maximum likelihood estimation method developed previously can now be used without the restriction that all the detectors are colocated because the time delays between the detectors can be computed using the known direction angles. Also, only two single-channel detectors are needed to solve the inverse problem in the known direction case, since there are only two unknowns, i.e., the two amplitudes associated with the two polarization states.

Assume the detection channels are identical with statistically independent Gaussian noise sources. The two complex response amplitudes A and B [see Eq. (3.7)] obtained from the ML estimator are

$$A = \frac{\left(\sum F_+^{(i)} y^{(i)}\right)\left(\sum F_\times^{(i)^2}\right) - \left(\sum F_\times^{(i)} y^{(i)}\right)\left(\sum F_+^{(i)} F_\times^{(i)}\right)}{\left(\sum F_+^{(i)^2}\right)\left(\sum F_\times^{(i)^2}\right) - \left(\sum F_+^{(i)} F_\times^{(i)}\right)^2} ,$$

$$B = \frac{\left(\sum F_\times^{(i)} y^{(i)}\right)\left(\sum F_+^{(i)^2}\right) - \left(\sum F_+^{(i)} y^{(i)}\right)\left(\sum F_+^{(i)} F_\times^{(i)}\right)}{\left(\sum F_+^{(i)^2}\right)\left(\sum F_\times^{(i)^2}\right) - \left(\sum F_+^{(i)} F_\times^{(i)}\right)^2} , \tag{4.32}$$

where the summations are over the channel number i.

A and B are Gaussian variables when the channel output $y^{(i)}$ is Gaussian because a linear combination of Gaussian variables produces another Gaussian variable [28]. From Eq. (4.32) it is apparent that the estimators of A and B are unbiased. The estimator variances are

$$V\{A\} = \frac{\sigma^2\left(\sum F_\times^{(i)^2}\right)}{\left(\sum F_+^{(i)^2}\right)\left(\sum F_\times^{(i)^2}\right) - \left(\sum F_+^{(i)} F_\times^{(i)}\right)^2} ,$$

$$V\{B\} = \frac{\sigma^2\left(\sum F_+^{(i)^2}\right)}{\left(\sum F_+^{(i)^2}\right)\left(\sum F_\times^{(i)^2}\right) - \left(\sum F_+^{(i)} F_\times^{(i)}\right)^2} , \tag{4.33}$$

where σ^2 is the noise variance of each channel. The estimator variances depend on the orientation factors and are independent of the signal amplitude.

2. *The minimum estimation error condition*

A condition for minimizing the estimation errors is found from Eq. (4.33) as

$$\sum F_+^{(i)}(\theta,\varphi) F_\times^{(i)}(\theta,\varphi) = 0 . \tag{4.34}$$

We refer to this condition as the "orthogonal channel configuration" because it requires that the two vectors $(F_+^{(1)},\ldots,F_+^{(N)})$ and $(F_\times^{(1)},\ldots,F_\times^{(N)})$ are orthogonal. Recall that $(F_+^{(1)},\ldots,F_+^{(N)})$ and $(F_\times^{(1)},\ldots,F_\times^{(N)})$ are the projections of the two polarization states of the wave on the detection channels.

The orthogonal channel condition cannot necessarily be satisfied for all direction angles (θ,φ). Only certain detector configurations and channel orientations will satisfy Eq. (4.34) for all direction angles. Recalling Eq. (3.3), Eq. (4.34) can be written in terms of the wave tensors and the detector tensors as

$$\sum_i F_+^{(i)}(\theta,\varphi) F_\times^{(i)}(\theta,\varphi) = \sum_i [D_{jk}^{(i)} W_+^{jk}(\theta,\varphi)][D_{lm}^{(i)} W_\times^{lm}(\theta,\varphi)] = 0 . \tag{4.35}$$

Substituting $W_+^{ij}(\theta,\varphi)$ and $W_\times^{ij}(\theta,\varphi)$ (Appendix B) into Eq. (4.35), the conditions for a detector network to satisfy Eq. (4.34), independent of the wave direction, are obtained:

$$\sum_i [(D_{11}^{(i)} - D_{33}^{(i)})^2 - (D_{11}^{(i)} - D_{33}^{(i)})(D_{22}^{(i)} - D_{33}^{(i)}) - 2D_{12}^{(i)^2}] = 0 ,$$

$$\sum_i [(D_{22}^{(i)} - D_{33}^{(i)})^2 - (D_{11}^{(i)} - D_{33}^{(i)})(D_{22}^{(i)} - D_{33}^{(i)}) - -2D_{12}^{(i)^2}] = 0 ,$$

$$\sum_i (D_{13}^{(i)^2} - D_{23}^{(i)^2}) = \sum_i D_{12}^{(i)} D_{13}^{(i)} = \sum_i D_{12}^{(i)} D_{23}^{(i)} = \sum_i D_{23}^{(i)} D_{13}^{(i)} = 0 , \tag{4.36}$$

$$\sum_i [(D_{11}^{(i)} - D_{33}^{(i)}) D_{12}^{(i)}] = \sum_i [(D_{11}^{(i)} - D_{33}^{(i)}) D_{13}^{(i)}] = \sum_i [(D_{11}^{(i)} - D_{33}^{(i)}) D_{23}^{(i)}] = 0 ,$$

$$\sum_i [(D_{22}^{(i)} - D_{33}^{(i)}) D_{12}^{(i)}] = \sum_i [(D_{22}^{(i)} - D_{33}^{(i)}) D_{13}^{(i)}] = \sum_i [(D_{22}^{(i)} - D_{33}^{(i)}) D_{23}^{(i)}] = 0 .$$

A spherical detector with the uncoupled transducer configuration discussed earlier satisfies Eq. (4.36) and thus achieves the minimum estimation error for any source direction.

The estimators and their variations are very simple in the case of the orthogonal channel configuration, namely,

$$A = \frac{\sum F_+^{(i)} y^{(i)}}{\sum F_+^{(i)^2}} \quad \text{and} \quad B = \frac{\sum F_\times^{(i)} y^{(i)}}{\sum F_\times^{(i)^2}} , \tag{4.37}$$

and the variances are

$$V\{A\} = \frac{\sigma^2}{\sum F_+^{(i)^2}} \quad \text{and} \quad V\{B\} = \frac{\sigma^2}{\sum F_\times^{(i)^2}} . \tag{4.38}$$

For a spherical detector these expressions can be simplified further using Eqs. (3.16) and (3.17):

$$A = \sum F_+^{(i)} y^{(i)} \quad \text{and} \quad B = \sum F_\times^{(i)} y^{(i)} , \tag{4.39}$$

and the variances are

$$V\{A\} = \sigma^2 \quad \text{and} \quad V\{B\} = \sigma^2 . \tag{4.40}$$

3. *The polarization factor*

Analogous to electromagnetic waves, the polarization state of a gravitational wave can be described with a polarization ellipse shown in Fig. 8. We introduce the polarization factor P, defined as the ratio of the area of the polarization ellipse to the energy flux of the wave, to describe the polarization ellipse. Let S be the area of the ellipse and E the wave energy flux, then

$$P \equiv 2\pi \frac{S}{E} = \frac{2h_{+0}h_{\times 0}|\sin(\phi_+ - \phi_\times)|}{h_{+0}^2 + h_{\times 0}^2} , \tag{4.41}$$

where h_{+0} and $h_{\times 0}$ are the amplitudes, and ϕ_+ and $\phi_\times$ are the phases of the two independent polarization states of the wave, respectively. The polarization factor is coordinate invariant, and it depends only on the phase difference and amplitude ratio of the two polarization states. $P = 0$ for a linearly polarized wave, and $P = 1$ for a circularly polarized wave.

Equivalently, P can be represented in terms of the response amplitudes A and B, since it depends only on the phase difference and amplitude ratio of the two polarization states. Thus,

$$P = \frac{2A_0B_0|\sin(\phi_A - \phi_B)|}{A_0^2 + B_0^2} , \tag{4.42}$$

where A_0 and B_0 are the amplitude and ϕ_A and ϕ_B are the phases of A and B, respectively.

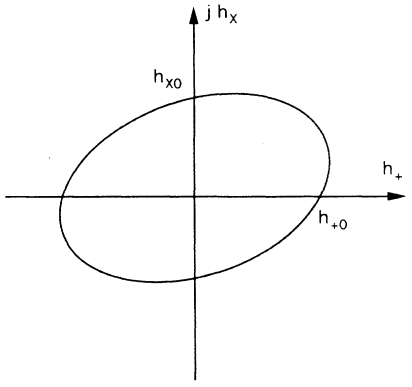

FIG. 8. Polarization ellipse of a gravitational wave.

$A(t)$ and $B(t)$ reflect the time dependence of $h_+(t)$ and $h_\times(t)$ when the frequency bandwidth of the detectors is larger than the bandwidth of the signal. We can study the time dependence of the wave polarization in that case. However, when the detector bandwidth is smaller than the signal bandwidth, Eq. (4.42) only applies when the polarization of the wave is time invariant.

In order to study the behavior of the polarization factor estimator in the presence of noise, Monte Carlo simulations of a spherical detector were done with 200 trials for each simulated input signal. Signals with different polarization states and signal-to-noise ratios were simulated. Five random complex numbers representing the effective noise of the five channels were drawn from an appropriate Gaussian distribution for each trial.

Figure 9 shows the mean and variance of the polarization factor estimator as functions of the signal-to-noise ratio. The polarization estimator is biased and tends to 0.5 at low signal-to-noise ratio. This bias is due to the nonlinear nature of the estimator. Only at relatively high signal-to-noise ratios is the polarization estimator a good estimator of the true polarization ellipse.

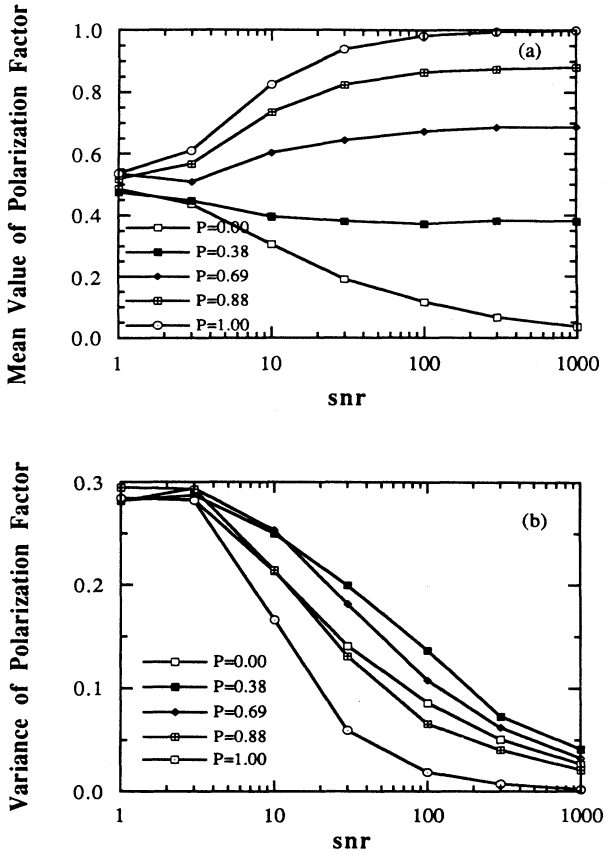

FIG. 9. Mean and variance of the polarization factor estimator obtained from numerical simulations. The estimator is clearly biased due to its nonlinear nature.

V. COINCIDENCE EXPERIMENTS WITH SPHERICAL DETECTORS

A coincidence experiment with two or more detectors is an efficient way to remove excess noise due either to the tail of a Gaussian distribution or to non-Gaussian disturbances [31]. Spherical detectors have additional advantages over other types of gravitational wave detectors in such coincidence experiments: (1) the direction resolution provides an additional criterion for discriminating against noise; (2) identical spherical detectors will register nearly the same amount of signal energy.

With regard to the second point, consider coincidence experiments with either cylindrical resonant-mass detectors or laser interferometric detectors. If these detectors are not all oriented in the same direction, they will, depending on the wave direction and polarization, register different signal energies for the same wave amplitude. Differences between the response amplitudes of the detectors in a coincidence experiment could be due either to local noise disturbances or to a real signal and therefore, there could be a large uncertainty in the signal amplitudes. Aligning all the detectors in the same direction can eliminate this ambiguity but it reduces the sky coverage. In contrast, identical spherical detectors will have nearly identical response amplitudes all within a range determined by the detector noise. This property can be used as an additional discriminator to eliminate false signals.

In the following we discuss the false-alarm probability and the detection probability. Along with the expected signal event rate, the false-alarm probability determines the detection threshold. The detection probability, which depends on the detection threshold, determines the detection sensitivity of a network of detectors. The rate of detectable signals can be estimated from the detection probability and the expected signal event rate. These estimates are made below for supernovae and binary coalescence events.

A. Energy distribution of a spherical detector

Consider a five-channel spherical detector in which the noise of each channel is independent and Gaussian with variance σ^2. The total output energy of such a detector is distributed as a χ^2 distribution [28] when no signal is present. The probability density function in this case is

$$P(E) = \frac{1}{(\sigma^2)^5\Gamma(5)}(E)^4 \exp\left[-\frac{E}{\sigma^2}\right] , \tag{5.1}$$

where E is the total energy output and E/σ^2 is the energy signal-to-noise ratio defined in Sec. IV A. The mean and the variance of E, determined from Eq. (5.1), are

$$E\{E\} = 5\sigma^2 ,$$
$$V\{E\} = 5\sigma^4 . \tag{5.2}$$

In the presence of a signal the detector energy is dis-

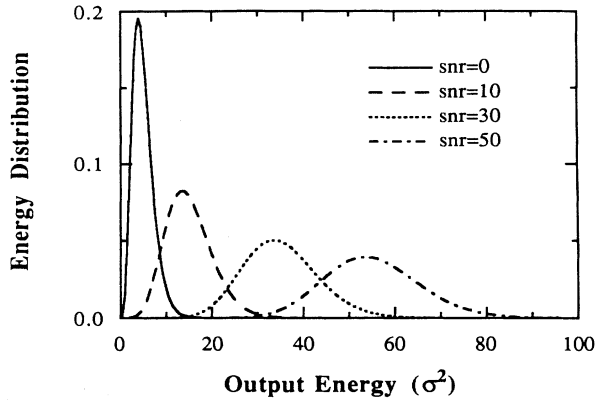

FIG. 10. Output energy distribution of a spherical detector with Gaussian noise. The noise variance is σ^2 for each channel.

tributed as a noncentral χ^2 distribution [28]:

$$P_S(E,E_S)=\frac{1}{\sigma^2}\left(\frac{E}{E_S}\right)^2 \times\exp\left(-\frac{E_S+E}{\sigma^2}\right)I_4(2\sqrt{E_SE}/\sigma^2)\ , \quad (5.3)$$

where E_S is the total signal energy and I_4 is the modified Bessel function of the first kind and order 4. The mean and the variance of E in this case are

$$E\{E\}=E_S+5\sigma^2\ ,$$
$$V\{E\}=4E_S\sigma^2+5\sigma^4\ . \quad (5.4)$$

Figure 10 shows the energy distribution for several values of the signal energy E_S. Both the mean and the variance of E increase with the total signal energy E_S.

B. False-alarm probability and detection threshold energy

Successful detection of a gravitational wave requires that all spherical detectors in a network have outputs above a given threshold and have the same output energy, arrival time, and estimated source direction within ranges determined by errors due to the presence of noise. In practice, the output of each detector must exceed a predetermined energy threshold within a time window determined by the maximum signal propagation time between the detectors. The distribution of the source direction estimates must also converge within a range determined by detector noise and signal strength.

1. False-alarm probability

The false-alarm probability is defined as the probability of an event satisfying the above energy and direction criteria without any signal present. It is simple to evaluate this probability when the detector noise is Gaussian.

The probability that the total output energy of a spherical detector exceeds the threshold energy E_0 in the absence of a signal is

$$p_e=1-\int_0^{E_0}P(E)dE\ , \quad (5.5)$$

where $P(E)$ is the energy distribution function given by Eq. (5.1). The threshold energy E_0 is usually set so that $p_e \ll 1$. The probability that a network of n detectors satisfies the energy criterion depends on the coincidence time window. If there are m data sampled during the allowed coincidence time window, the probability of a detector having one output data higher than the threshold energy within the coincidence window is approximately mp_e and therefore the probability that an n-detector network accidentally satisfies the energy criterion is $(mp_e)^n$.

The coincidence window m depends on the uncertainties in the signal propagation times between the detectors. m is usually a small number because the maximum propagation delay is about 42 ms and the typical sampling time for a resonant-mass detector is about 100 ms. For a colocated detector network, $m=1$.

Now consider the probability of the direction criterion being accidentally satisfied. For $S/N=10$, in 90% of all trials the direction estimate deviates from the true wave direction by less than 0.5 rad and so the angles between different direction estimates are less than 1 rad. The higher the signal-to-noise ratio, the smaller the average angular deviation. In the following we require that the direction estimates obtained from the detectors in the network differ by less than $\beta=1$ rad. When $S/N>10$, more than 90% of the direction estimates should satisfy this criterion.

A network of n detectors generates n estimated source directions for each event. For a real signal, nearly all the estimated directions should be inside a circle of radius $\beta/2$ on a unit celestial sphere. The true source location will be at the center of the circular area when n is large. The angle between the true wave direction and any of the estimated direction is less than $\beta/2$, and the angle between any two estimated directions is less than β for more than 90% of the points. The area of the circular error box is

$$S_0=2\pi[1-\cos(\beta/2)]\ . \quad (5.6)$$

When no signal is present, the estimated source directions will be randomly distributed over the sky. The accidental probability that all the estimated locations are inside a circle with area S_0 is

$$p_a=\left(\frac{S_0}{2\pi}\right)^{n-1}=[1-\cos(\beta/2)]^{n-1}\ . \quad (5.7)$$

The denominator in Eq. (5.7) is 2π instead of 4π because a spherical detector cannot distinguish diametrically opposite points in the sky.

For $\beta=1.0$ rad, the accidental probability is

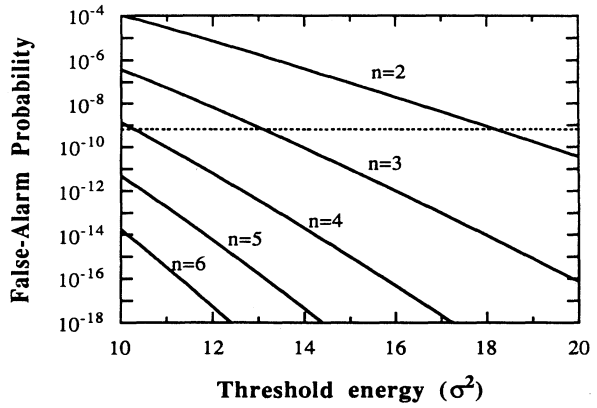

FIG. 11. False-alarm probability vs the detection threshold energy. n is the number of detectors in the network.

$$p_a = (1-\cos 0.5)^{n-1} = (0.1224)^{n-1} . \quad (5.8)$$

Combining the accidental probability of all detectors passing the energy threshold test and the accidental probability that all the estimated source directions are inside an error box with area S_0, we obtain the false-alarm probability for a network of n spherical detectors as

$$p_f = (mp_e)^n (0.1224)^{n-1} = m^n \left(1 - \int_0^{E_0} P(E)dE\right)^n (0.1224)^{n-1} . \quad (5.9)$$

Figure 11 shows the false-alarm probability versus the threshold energy for different numbers of detectors operated in coincidence. We have used $m = 1$ in the calculation. The false-alarm probability exponentially decreases with increasing threshold energy. It also dramatically decreases as the number of detectors increases. For example, when the threshold energy is set to $10\sigma^2$, $p_f \approx 10^{-4}$ for a two-detector network, 3×10^{-7} for a three-detector network, and 10^{-9} for a four-detector network.

2. Detection threshold energy

The threshold energy E_0 should be set so that the false-alarm rate is much less than the detectable signal occurrence rate. The occurrence rate of detectable gravitational waves depends not only on the occurrence rate of impulsive gravitational wave signals but also on the strength of the signals produced. The detectable signal event rate is uncertain at present but is likely to be very low even for advanced spherical detectors as we will see later. Optimistic estimates for the rate of detectable gravitational radiation signals are about several events per year.

For the optimistic rates, the detection threshold energy E_0 can be set so that the probability of having a false-alarm event in $\frac{1}{3}$ year is less than 0.1. Then when there is an event satisfying the detection criteria discussed above in $\frac{1}{3}$ year, we can have more than 90% confidence that the event is not due to the detector noise but a real gravitational wave signal.

Assume the sampling rate is once per 0.15 s. There are then 5.76×10^5 samples per detector per day, resulting in $M = 7.0 \times 10^7$ events per $\frac{1}{3}$ year. The probability that none of the M events is a false-alarm event is

$$p_1 = (1-p_f)^M . \quad (5.10)$$

90% confidence of detection requires p_1 equal 0.9, which leads to $p_f = 6.5 \times 10^{-10}$ for $M = 7.0 \times 10^7$ events. In Fig. 5 this threshold of the false-alarm probability is shown as the dashed line.

We can then set the threshold energy according to the p_f required. For $p_f \approx 10^{-9}$, the energy threshold is $18.1\sigma^2$ for two detectors operating in coincidence, $13.0\sigma^2$ for three detectors, and $10.3\sigma^2$ for four detectors.

3. Non-Gaussian disturbances

Based on experience with cylindrical resonant-mass detectors, we can reasonably expect about 1–3 non-Gaussian events per day which will cause the output of a single detector to exceed the energy threshold. For a detector network, the false-alarm probability due to non-Gaussian noise is

$$p'_f = (p'_e)^n (0.1224)^{n-1} , \quad (5.11)$$

where n is the number of detectors, and p'_e is the occurrence probability of a non-Gaussian event. p'_e is equal to the number of non-Gaussian events per day divided by the total number of events per day. For a sampling time of 0.15 s, $p'_e = 1.74 \times 10^{-6}$ for the case of one non-Gaussian event per day. Table V shows the false-alarm probability due to non-Gaussian disturbances for various detector networks.

Clearly, a coincidence experiment is an efficient way to eliminate non-Gaussian disturbances. For the case of one non-Gaussian event per day per detector, the false-alarm probability is much less than 6.5×10^{-10}, which is the false-detection probability required for 90% confidence in detecting a signal in $\frac{1}{3}$ year in the presence of Gaussian noise alone.

TABLE V. False-alarm probability due to non-Gaussian disturbances.

Number of detectors	p'_f = 1 event/day	p'_f = 100 events/day
2	3.7×10^{-13}	3.7×10^{-9}
3	7.9×10^{-20}	7.9×10^{-14}
4	1.7×10^{-26}	1.7×10^{-18}

C. Detection probability

1. Detection probability

The detection probability is defined as the probability that all the detector outputs exceed a given threshold when a signal is present. It depends on both the signal energy and the detection threshold energy.

Recall that the distribution function for the energy output of a spherical detector is a noncentral χ^2 distribution $P_S(E, E_S)$ when a signal is present. The probability that a detector exceeds threshold energy E_0 when a signal is present is

$$p_D^{(1)}(E_S) = \int_{E_0}^{\infty} P_S(E, E_S) dE \ . \tag{5.12}$$

The detection probability for an n-detector network is then

$$p_D^{(n)}(E_S) = [p_D^{(1)}(E_S)]^n = \left[\int_{E_0}^{\infty} P_S(E, E_S) dE\right]^n = \left[1 - \int_0^{E_0} P_S(E, E_S) dE\right]^n . \tag{5.13}$$

Figure 12 shows the detection probabilities versus the signal energy for a detector network with different numbers of detectors. The energy threshold has been set so that the probability of false alarm is less than 10% in $\frac{1}{3}$ year. Note that a signal with a total amount of energy larger than the detection threshold energy could be missed by a network of detectors, and a signal with a total amount of energy smaller than the threshold energy still has a chance of being detected. Consider a three-detector network whose threshold energy is $13.0\sigma^2$ as an example. 70% of signals with total energy of $15\sigma^2$ can be detected and 22% of signals with total energy of $10\sigma^2$ can also be detected.

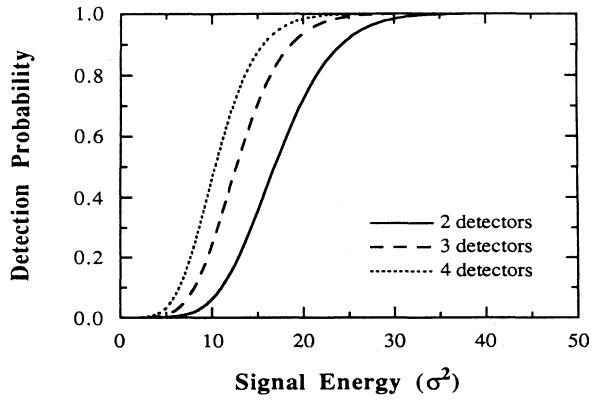

FIG. 12. Detection probability vs signal energy. The energy threshold has been set so that the probability of false alarm is less than 10% in $\frac{1}{3}$ year.

2. Detectable signal event rate

We can now estimate the event rate of detectable gravitational wave signals for a network of spherical detectors. Assume that the gravitational wave sources are standard candles that emit $\eta(R)$ pulses of gravitational radiation per unit volume per year and that each pulse has energy $E_{\rm GW}$. The average signal energy deposited in a spherical antenna by each pulse depends on the source distance R as

$$E_S = \frac{dE_{\rm GW}(f_0)}{df} \frac{\Sigma}{4\pi R^2} \ , \tag{5.14}$$

where $\Sigma = \int \sigma(f) df$, is the frequency integral of the energy cross section of the spherical antenna and $dE_{\rm GW}(f_0)/df$ is the radiation energy per unit frequency at the resonant frequency of the antenna averaged over direction. Equation (5.14) of course assumes that the signal pulse bandwidth is broad compared to the resonant width of the antenna.

The probability of an n-detector network detecting such a signal is $p_D^{(n)}(E_S)$. There are $4\pi R^2 \eta(R) \Delta R$ signal pulses emitted each year in a shell of radius R and thickness ΔR. The rate of detectable signals due to the sources in that shell is then $p_D^{(n)}(E_S)\eta(R)4\pi R^2 \Delta R$, and the total detectable signal event rate is therefore given by

$$r = 4\pi \int_0^{\infty} p_D^{(n)}(E_S)\eta(R) R^2 dR \ . \tag{5.15}$$

Equation (5.15) can be simplified if the signal sources are assumed to uniformly fill the space such that $\eta(R) = \eta$, independent of the source distance R. Changing variables of integration by using Eq. (5.14), we rewrite Eq. (5.15) as

$$r = \eta \frac{1}{\sqrt{4\pi}} \left[\frac{dE_{\rm GW}(f_0)}{df} \Sigma\right]^{3/2} \int_0^{\infty} \frac{p_D^{(n)}(E_S)}{E_S^{5/2}} dE_S \ . \tag{5.16}$$

We referred to $p_D^{(n)}(E_S)/E_S^{5/2}$ as the detectable-signal density function. Figure 13 shows this function for three- and four-detector networks. The detectable-signal density peaks just above the detection threshold energy. This is easily understood as follows. In the case of low E_S the signal sources are relatively far away. There are a relatively large number of sources, but $p_D^{(n)}(E_S)$ is very small so that the detectable-signal density is low. In the other extreme case, a nearby source will deposit a large amount of energy in the detector but there are relatively few sources nearby. The detectable-signal density is therefore also very low in this case because of the low occurrence rate of signals.

Evaluating the integral in Eq. (5.16) gives the detectable-signal event rates,

$$r = 4.8 \times 10^{-3} \eta \left[\frac{dE_{\rm GW}(f_0)}{df} \frac{\Sigma}{\sigma^2}\right]^{3/2} \tag{5.17}$$

for a three-detector network and

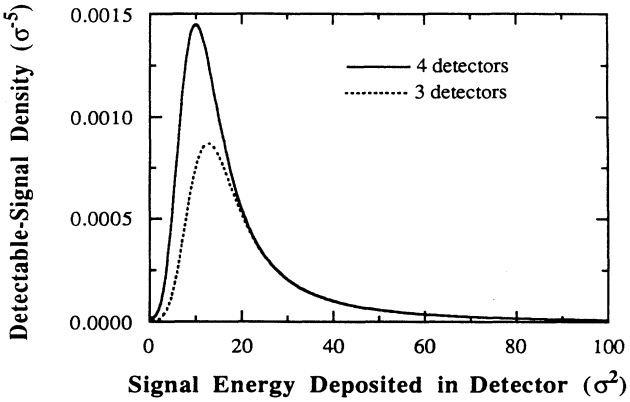

FIG. 13. Detectable-signal density function defined in the text. The detection threshold energy is $13.0\sigma^2$ for a three-detector network and $10.3\sigma^2$ for a four-detector network.

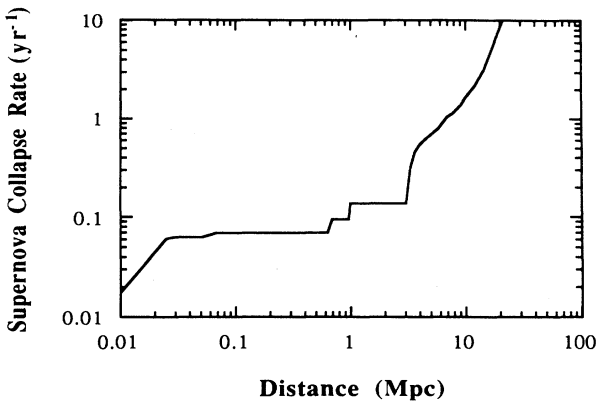

FIG. 14. Supernova core collapse rate as functions of distance. The data are obtained assuming that the supernova collapse rate is proportional to star population and within our galaxy the rate is once per 40 years. The rate is three per year out to the distance of Virgo and increases proportional to (distance)^3 beyond that distance.

$$r = 6.8 \times 10^{-3}\eta \left[\frac{dE_{\rm GW}(f_0)}{df}\frac{\Sigma}{\sigma^2}\right]^{3/2} \tag{5.18}$$

for a four-detector network where σ^2 is the noise variance of an individual detector. The detectable-signal event rate depends on the occurrence rate of the signal as well as the amount of energy emitted by the source at the resonant frequency of the detector. It also depends on the energy cross section and the noise variance of the detector. If the energy cross section is increased by 100 times, as in the case of high sound velocity material antenna [15], the detectable-signal event rate is increased by 1000 times.

D. Event rate of detectable supernovae

Estimation of the event rate of detectable supernovae requires estimates of the occurrence rate and the gravitational wave signal strength of supernovae. However, both estimates have large uncertainties at present. The strength of the gravitational waves from a supernova depends crucially on the degree of nonsphericity in the stellar collapse that triggers it [32]. A perfectly spherical collapse will produce no waves, while a highly nonspherical collapse can produce strong waves. Little is actually known about the degree of nonsphericity in supernova collapses, and theoretical predictions of the total gravitational radiation energy emitted vary from $\Delta E_{\rm GW} \approx 10^{-2}M_\odot c^2$ to $\Delta E_{\rm GW} \approx 10^{-7}M_\odot c^2$ or lower [32]. Predictions of the wave forms are also poor, but the characteristic frequency of the waves f_c is widely believed to be around 1000 Hz [32].

If the frequency bandwidth of the signal is taken to be about the same as the characteristic frequency f_c, the gravitational wave energy per unit frequency can be roughly estimated as

$$\frac{dE_{\rm GW}(f_0)}{df} = \frac{E_{\rm GW}}{f_c} . \tag{5.19}$$

The occurrence rate of supernovae in our galaxy is observationally estimated [32,33] as roughly one type-I and one type-II supernova per 40 years. Assuming this occurrence rate is proportional to the star population, then out to the distance of the center of the Virgo cluster of galaxies several type-I and several type-II supernovae occur each year. The rate increases as (distance)^3 near and beyond Virgo. Figure 14 shows the supernovae collapse rate as a function of source distance [34].

From Fig. 14 and Eq. (5.15) we can estimate the detectable event rate for supernovae. Table VI shows the estimates for a network of four aluminum spherical detectors operating at the quantum limit. If the gravitational radiation energy emitted by a supernova is $E_{\rm GW} \sim 10^{-8}M_\odot c^2$, the detector sensitivity is only sufficient to detect the sources within our galaxy and the detectable event rate is about once per 60 years. The detectable event rate slightly increases as $E_{\rm GW}$ increases until the detector sensitivity allows detection of sources near Virgo. Once $E_{\rm GW}$ is this large, the detectable event increases proportional to $(E_{\rm GW})^{3/2}$. For

TABLE VI. The estimated event rate of detectable supernovae for a network of four aluminum spherical detectors operating at the quantum limit.

$E_{\rm GW}(M_\odot c^2)$	10^{-2}	10^{-4}	10^{-6}	10^{-8}
Event rate (yr^{-1})	5.8	0.14	0.069	0.015

$E_{GW} \sim 10^{-2} M_\odot c^2$, a quantum-limited four-detector network could detect sources as far as 16 Mpc at a rate of about six per year.

The detectable event rate also crucially depends on the detector energy cross section. If the antennas are made of high sound velocity material and have 100 times larger energy cross section compared to aluminum antennas [15], the detectable event rate could reach several per year for $E_{GW} \sim 10^{-4} M_\odot c^2$.

E. Event rate of detectable binary coalescences

A compact binary system formed by neutron stars or black holes will eventually be driven into coalescence by gravitational radiation reaction [32]. As the two bodies in a compact binary spiral together, they emit a quasiperiodic chip of gravitational radiation with a frequency sweeping upward toward a maximum frequency. During the final stage of coalescence the system will likely produce an intense burst of gravitational waves.

The inspiral stage of coalescence has been studied and the Newtonian-order wave forms, which are of sufficient accuracy for our purpose [35], are given by [36]

$$h_+(t) = 2(1+\cos^2\zeta)(\mu/R)(\pi M f)^{2/3} \times \cos\left(2\pi \int_{t_a}^{t} f(t')dt' + \Phi\right) ,$$
$$h_\times(t) = 4\cos\zeta(\mu/R)(\pi M f)^{2/3} \times \sin\left(2\pi \int_{t_a}^{t} f(t')dt' + \Phi\right) , \quad (5.20)$$

where t_a is an arbitrary defined initial time, Φ is the signal's phase at time t_a, ζ is the angle of inclination of the circular orbit to the line of sight, M and μ are the total and reduced masses, respectively, and f, the frequency of the waves, is given by

$$f = \frac{1}{\pi}\left[\frac{5}{256}\frac{1}{\mu M^{2/3}}\frac{1}{(t-t_0)}\right]^{3/8} , \quad (5.21)$$

where $t - t_0$ is the retarded time. The Fourier transform is [32]

$$\langle|\tilde{h}_+|^2 + |\tilde{h}_\times|^2\rangle = \frac{\pi}{12}\left(\frac{\mu}{R}\right)^2 \frac{M^2}{\mu}\frac{1}{(\pi M f)^{7/3}} , \quad (5.22)$$

where the average is over the source orientation angle ζ. In Eqs. (5.20), (5.21), and (5.22) units with $c = G = 1$ have been used.

The total radiation energy per unit frequency from a coalescing binary system is, from Eq. (5.22),

$$\frac{dE_{GW}}{df} = (4\pi R^2)\frac{\pi}{2}\frac{c^3}{G} f^2 \langle|\tilde{h}_+|^2 + |\tilde{h}_\times|^2\rangle = \frac{\pi^{2/3}}{6} G^{2/3} M^{2/3} \mu f^{-1/3} . \quad (5.23)$$

In Eq. (5.23) we have restored the conventional units.

TABLE VII. Detectable event rate estimates for binary coalescences.

R_0 (Mpc)	23	200	1000
Event rate (yr^{-1}) (NS-NS)	3.8	5.7×10^{-3}	4.6×10^{-5}
Event rate (yr^{-1}) (BH-NS)	35.5	0.054	4.32×10^{-4}
Event rate (yr^{-1}) (BH-BH)	519	0.79	6.32×10^{-3}

The radiation signal strength depends on the masses of objects in the binary system.

As in the case of supernovae, the occurrence rate estimates for binary coalescences also have large uncertainties. Narayan, Piran, and Shemi [37] and Phinney [38] have estimated the binary coalescence rate based on observations of binary pulsars [39–42]. For neutron star binaries (NS-NS), a very conservative lower limit to the merger rate is three per year within 1 Gpc; the best, but still conservative, estimate is three per year within 200 Mpc; and a somewhat optimistic upper limit is three per year within 23 Mpc (assuming a Hubble constant of 100 $km\,s^{-1}\,Mpc^{-1}$). The merger rates for black-hole–neutron-star (BH-NS) and black-hole–black-hole (BH-BH) binaries are believed to be comparable to that for NS-NS binaries [38].

Assuming that the binary sources are uniformly distributed in space (at least on scales of 100 Mpc), Table VII shows the estimated detectable event rates for several binary systems. In Table VII R_0 is the distance within which three mergers occur per year. The detector system is assumed to be a network of four aluminum spherical detectors operating at the quantum limit. The masses of neutron stars and black holes are assumed to be $1.4M_\odot$ and $10M_\odot$, respectively.

Clearly, the estimates of detectable event rates depend strongly on the binary merger rate, varying by several orders of magnitude between the most conservative and the optimistic estimates. Note that the burst from the final stage of coalescence has not been taken into account in these estimates because so little is known about it. The final coalescence burst might deposit a considerable amount of energy in a resonant-mass detector so that the actual detectable-signal event rate might be higher than what we have estimated above.

VI. SUMMARY

A spherical antenna, with five degenerate quadrupole modes that can interact with gravitational radiation, has an energy cross section that is independent of the direction and the polarization of the incoming wave and is much larger than that of a cylindrical antenna made of the same material and with the same resonant frequency. The antenna readout requires at least five transducers to monitor the five quadrupole modes. In principle, five transducers can be mounted on the surface of the sphere, with each coupled to one and only one of

the five modes. With this arrangement a single spherical detector is equivalent to five independent single-channel detectors.

A single spherical detector can provide source direction estimates. By using the maximum likelihood estimation method, an algorithm for solving the inverse problem with a spherical detector in the presence of noise has been developed. The direction estimation errors have also been evaluated both numerically and analytically. A spherical detector has a reasonable direction resolution even at relatively low signal-to-noise ratio ($S/N = 10$, or an average single channel amplitude $S/N = 1.4$), while an interferometer network requires a much higher S/N for direction estimation. A spherical detector has isotropic direction resolution independent of the source direction and polarization, in contrast to the interferometer network, which can only partially cover the sky. A comparison of a spherical detector operating at 50-mK temperature and a network of three interferometers with the projected sensitivity of the initial LIGO detectors shows that over about 65% of the sky the spherical detector has better direction resolution.

The direction resolution and isotropic detection sensitivity give a network of spherical detectors additional advantages in performing coincidence experiments. By studying the false-alarm and detection probabilities, we have estimated the event rates of detectable gravitational wave signals from supernovae and binary coalescences for a network of four aluminum spherical detectors operating at the quantum limit. For supernovae, an optimistic estimate that assumes the gravitational radiation signal energy is large enough ($E_{\rm GW} \sim 10^{-2} M_\odot$) to allow detection of sources near or beyond Virgo gives an event rate of several per year, while a more pessimistic estimate that assumes $E_{\rm GW}$ is so small that only the sources within our galaxy can be detected gives an event rate of about one per 60 years. For the case of binary coalescence signals, the detectable event rates exceed several per year for the optimistic estimates; for the best, but still conservative, estimates the detectable BH-BH binary coalescence rate is about one per year, while detectable NS-NS and BH-NS coalescence rates are only one per 175 and 18 years, respectively.

The above estimates are based on the assumption that the detectors operate at the quantum limit. In fact, detectors are more likely to operate at a noise level ~ 10 times higher than the quantum limit in the near future [16]. For these detectors the optimistic estimate of the detectable event rate for supernovae is about one per year (the detectors can detect sources at distances as far as 9 Mpc for $E_{\rm GW} \sim 10^{-2} M_\odot$) and a pessimistic estimate is that the detectors can detect sources only within our galaxy. For detection of binary coalescences the optimistic estimates are that the event rates are once per 10 yr for NS-NS binaries, once per year for BH-NS binaries, and 16 per year for BH-BH binaries.

Although the quantum limit represents a likely practical lowest noise level for resonant-mass detectors, the above estimates for detectors operating at the quantum limit do not represent the ultimate detection limit for spherical detectors because the detectable event rate depends strongly on the detector energy cross section which, in turn, can be greatly improved by optimizing the antenna material.

Using high sound velocity material for the antenna can greatly increase the energy cross section [15]. The energy cross section is proportional to the fifth power of the sound velocity for a fixed resonant frequency. For example, the energy cross section of an antenna made of silicon carbide can be about 100 times larger than that of an aluminum antenna [15]. The detectable event rate is proportional to $\Sigma^{3/2}$ if the sources are uniformly distributed. Thus a 100-fold increase in the energy cross section will result in a 1000-fold increase in the detectable event rates.

Low resonant frequency detectors can also have larger energy cross sections, since the energy cross section is inversely proportional to the cubic of the resonant frequency. Besides this, they also have additional advantages in detecting gravitational waves, namely, (1) the higher frequency quadrupole modes of a spherical antenna can be used to detect gravitational waves and (2) the low frequency antenna has higher sensitivity to the binary coalescence signals because the radiation energy per unit frequency is proportional to $f^{-1/3}$ [see Eq. (5.23)]. Consider two detectors, one with a resonant frequency near 1 kHz and the other with a resonant frequency half of that. The lower resonant frequency detector has about 10 times larger signal energy than the higher frequency one in detecting binary coalescence signals.

The ultimate detector network might consist of four spherical detectors operating at the quantum limit with high sound velocity materials used for the antennas and resonant frequency ~ 400 Hz. This detector network could detect supernova signals more than once per year if the gravitational radiation energy is larger than $4 \times 10^{-5} M_\odot$. This network could also detect binary coalescence signals at a rate of more than one per year even for the most conservative estimate of a binary coalescence rate of three per year within 1 Gpc.

ACKNOWLEDGMENTS

We would like to thank R. Penny, L. Mann, W. O. Hamilton, H. J. Paik, W. Johnson, N. Solomonson, T. Stevenson, and M. Cerdonio for helpful discussions. This work was supported by the National Research Foundation under Grant No. PHY 92-20530.

APPENDIX A: RESPONSES OF TOROIDAL QUADRUPOLE MODES TO A GRAVITATIONAL WAVE

According to general relativity, a gravitational radiation field is a tensor field of massless spin-2 particles. In the wave-based coordinate system, the nonvanishing components of the Riemann tensor are [11]

$$R_{x0x0} = -R_{y0y0} = -\frac{1}{2}\frac{\partial^2}{\partial t^2} h_+ \ , \tag{A1}$$

$$R_{x0y0} = R_{y0x0} = -\frac{1}{2}\frac{\partial^2}{\partial t^2}h_\times \ ,$$

where h_+ and $h_\times$ are the gravitational wave amplitudes of the two independent polarization states. The mode driving force is given by [10]

$$R_n(t) = -M^{-1}R_{i0j0}(t)\int \Psi_n^{i^*}x^j\rho\, d^3x \ , \tag{A2}$$

where ρ and M are the density and mass of the antenna, and Ψ_n is the eigenfunction of the nth normal mode. The coordinate origin is taken to be the center of mass of the antenna.

For toroidal modes, Ψ_n is given by [9]

$$\Psi_{lm} = C\psi_l(\kappa r)(\mathbf{r}\times\nabla Y_{lm}) \ , \tag{A3}$$

where C is the normalized amplitude, $Y_{lm}(\theta,\varphi)$ are spherical harmonics. $\kappa^2 = \rho\omega_l^2/\mu$, where ω_l is the resonant frequency of the normal mode and μ is the shear modulus. $\psi_l(x)$ is a function given by

$$\psi_l(x) = \left(\frac{1}{x}\frac{d}{dx}\right)^l\left(\frac{\sin x}{x}\right) \ . \tag{A4}$$

Substituting Eqs. (A1) and (A3) into Eq. (A2), the mode driving force is obtained as

$$\begin{aligned} R_{lm} &= \frac{3C}{8\pi R^3}\int_0^R r^2\,dr\int_0^\pi \sin\theta\,d\theta\int_0^{2\pi} d\varphi\,\psi_l(\kappa r)[\ddot{h}_+(x\hat{\mathbf{e}}_x - y\hat{\mathbf{e}}_y)\cdot(r\times\nabla Y_{lm}^*) + \ddot{h}_\times(y\hat{\mathbf{e}}_x + x\hat{\mathbf{e}}_y)\cdot(r\times\nabla Y_{lm}^*)] \\ &= -\frac{3C}{8\pi R^3}\int_0^R \psi_l(\kappa r)r^3dr\int_0^\pi \sin\theta\,d\theta\int_0^{2\pi} d\varphi\left[\ddot{h}_+\left(\sin\theta\,\sin 2\varphi\frac{\partial Y_{lm}^*}{\partial\theta} + \cos\theta\,\cos 2\varphi\frac{\partial Y_{lm}^*}{\partial\varphi}\right)\right. \\ &\quad \left. +\ddot{h}_\times\left(-\sin\theta\,\cos 2\varphi\frac{\partial Y_{lm}^*}{\partial\theta} + \cos\,\sin 2\varphi\frac{\partial Y_{lm}^*}{\partial\varphi}\right)\right] \ . \end{aligned} \tag{A5}$$

Using Legendre functions, $\partial Y_{lm}^*/\partial\theta$ and $\partial Y_{lm}^*/\partial\varphi$ can be expressed as

$$\begin{aligned} \frac{\partial Y_{lm}^*}{\partial\theta} &= (-1)^m\left[\frac{2l+1}{4\pi}\frac{(l-m)!}{(l+m)!}\right]^{1/2}\frac{\partial P_l^m(\cos\theta)}{\partial\theta}e^{-im\varphi} \ , \\ \frac{\partial Y_{lm}^*}{\partial\varphi} &= -im(-1)^m\left[\frac{2l+1}{4\pi}\frac{(l-m)!}{(l+m)!}\right]^{1/2}P_l^m(\cos\theta)e^{-im\varphi} \ , \end{aligned} \tag{A6}$$

where $P_l^m(\cos\theta)$ is the Legendre function. From Eqs. (A5) and (A6) we see that each term of the integral in Eq. (A5) contains either $\int_0^{2\pi}\sin 2\varphi\, e^{-im\varphi}d\varphi$ or $\int_0^{2\pi}\cos 2\varphi\, e^{-im\varphi}d\varphi$. These integrals are zero except for $m = \pm 2$ as

$$\begin{aligned} \int_0^{2\pi}\cos 2\varphi\, e^{-im\varphi}d\varphi &= \begin{cases} \pi, & m = \pm 2 \ , \\ 0, & \text{others} \ , \end{cases} \\ \int_0^{2\pi}\sin 2\varphi\, e^{-im\varphi} &= \begin{cases} -i\pi, & m = 2 \ , \\ i\pi, & m = -2 \ , \\ 0, & \text{others} \ . \end{cases} \end{aligned} \tag{A7}$$

Thus, the normal-mode driving force due to gravitational waves are zero except for $m = \pm 2$ modes. For $m = \pm 2$, the mode driving force can be written as

$$R_{lm} = A_l(i\ddot{h}_+ \pm \ddot{h}_\times)\int_0^R \psi_l(\kappa r)r^3\,dr\int_{-1}^{+1} du\left[2u + (u^2-1)\frac{d}{du}\right]P_l^m(u), \quad m = \pm 2 \tag{A8}$$

where $u = \cos\theta$ and A_l is a constant as

$$A_l = \frac{3C}{8R^3}\left[\frac{2l+1}{4\pi}\frac{(l+2)!}{(l-2)!}\right] \ . \tag{A9}$$

Using the recurrence relation of Legendre functions that

$$(1-u^2)\frac{d}{du}P_l^m = -luP_l^m + (l+m)P_{l-1}^m, \tag{A10}$$

Eq. (A8) is rewritten as

$$R_{lm} = A_l(l+2)(i\ddot{h}_+ \pm \ddot{h}_\times)\int_0^R \psi_l(\kappa r) r^3 dr \int_{-1}^{+1} du[uP_l^m(u) - P_{l-1}^m(u)], \quad m = \pm 2 \ . \tag{A11}$$

It is easy to verify that for quadrupole modes $l = 2$, $R_{lm} = 0$. In fact, for even l, the integral $\int_{-1}^{+1} du[up_l^2 - P_{l-1}^2] = 0$. This can be seen as follows.

$P_2^2 = 3(1-u^2)$ is an even function and $P_3^2 = 15u(1-u^2)$ is an odd function of u. Assuming that P_{l-1}^2 is an odd function and P_{l-2}^2 is an even function, we observe that P_l^2 is an even function from the following recurrence relation:

$$(l-m)P_l^m = (2l-1)uP_{l-1}^m - (l-1+m)P_{l-2}^m \ . \tag{A12}$$

Similarly, if P_{l-1}^2 is an even function and P_{l-2}^2 is an odd function, then P_l^2 is an odd function. Therefore, for even l, P_l^2 is an even function and for odd number l, P_l^2 is an odd function. For even l, the integral $\int_{-1}^{+1} du[up_l^2 - P_{l-1}^2] = 0$ because the integrand is an odd function of u and therefore, gravitational wave driving forces are zero.

APPENDIX B: SYMMETRIC-TRACE-FREE (STF) WAVE TENSORS [7,8]

Consider a plane gravitational wave with amplitudes $h_+(t)$ and $h_\times(t)$ associated with the two independent polarizations. In the wave coordinate system, where the wave travels in the z direction, the wave tensor $h_{ij}(t)$ has the nonvanishing components

$$\begin{aligned} h_{xx} &= -h_{yy} = h_+(t) \ , \\ h_{xy} &= h_{yx} = h_\times(t) \ . \end{aligned} \tag{B1}$$

The wave tensor is symmetric and trace free.

$h_{ij}(t)$ can also be represented with a null vector $\mathbf{m}$,

$$\begin{aligned} h_{ij} &= 2h_+(t)\mathrm{Re}(m_i m_j) + 2h_\times(t)\mathrm{Im}(m_i m_j) \\ &= h_+(t)W_{+ij} + h_\times(t)W_{\times ij} \ , \end{aligned} \tag{B2}$$

where the null vector $\mathbf{m}$ is

$$\mathbf{m} = \frac{1}{\sqrt{2}}(\hat{\mathbf{e}}_x + i\hat{\mathbf{e}}_y) \ . \tag{B3}$$

W_{+ij} and $W_{\times ij}$ are also symmetric and trace-free tensors given by

$$\begin{aligned} W_{+ij} &= 2\mathrm{Re}(m_i m_j) \ , \\ W_{\times ij} &= 2\mathrm{Im}(m_i m_j) \ . \end{aligned} \tag{B4}$$

In the laboratory coordinate system, the null vector $\mathbf{m}$ becomes

$$\begin{aligned} \mathbf{m} = \frac{1}{\sqrt{2}}[&(\cos\varphi - i\cos\theta\sin\varphi)\hat{\mathbf{e}}_{x'} \\ &+(\sin\varphi + i\cos\theta\cos\varphi)\hat{\mathbf{e}}_{y'} + (i\sin\theta)\hat{\mathbf{e}}_{z'}] \ , \end{aligned} \tag{B5}$$

where $\hat{\mathbf{e}}_{x'}$, $\hat{\mathbf{e}}_{y'}$, and $\hat{\mathbf{e}}_{z'}$ are unit vectors in the laboratory frame. θ and φ are the usual Euler angles. The third Euler angle ψ has been set equal to zero. This choice is a convention for identifying $h_+(t)$ and $h_\times(t)$, since ψ merely determines the orientation of the wave frame's (x,y) axes in the x-y plane and has no effect on any results.

W_{+ij} and $W_{\times ij}$ are found from Eqs. (B4) and (B5) in the laboratory coordinate system. They are

$$W_+ = \begin{bmatrix} \cos^2\varphi - \cos^2\theta\sin^2\varphi & \frac{1}{2}\sin 2\varphi(1+\cos^2\theta) & \frac{1}{2}\sin 2\theta\sin\varphi \\ \frac{1}{2}\sin 2\varphi(1+\cos^2\theta) & \sin^2\varphi - \cos^2\theta\cos^2\varphi & -\frac{1}{2}\sin 2\theta\cos\varphi \\ \frac{1}{2}\sin 2\theta\sin\varphi & -\frac{1}{2}\sin 2\theta\cos\varphi & -\sin^2\theta \end{bmatrix} \ , \tag{B6}$$

$$W_\times = \begin{bmatrix} -\cos\theta\sin 2\varphi & \cos\theta\cos 2\varphi & \sin\theta\cos\varphi \\ \cos\theta\cos 2\varphi & \cos\theta\sin 2\varphi & \sin\theta\sin\varphi \\ \sin\theta\cos\varphi & \sin\theta\sin\varphi & 0 \end{bmatrix} \ .$$

APPENDIX C: THE TRANSFORMATION MATRIX $T_{n,m}(\theta,\varphi)$

$$T_{0,0}=\tfrac{3}{2}\cos^2\theta-\tfrac{1}{2},\quad T_{0,1c}=-\frac{\sqrt{3}}{2}\sin 2\theta\cos\varphi,\quad T_{0,1s}=\frac{\sqrt{3}}{2}\sin 2\theta\sin\varphi\ ,$$

$$T_{0,2c}=\frac{\sqrt{3}}{2}\sin^2\theta\cos 2\varphi,\quad T_{0,2s}=-\frac{\sqrt{3}}{2}\sin^2\theta\sin 2\varphi\ ,$$

$$T_{1c,0}=\frac{\sqrt{3}}{2}\sin 2\theta,\quad T_{1c,1c}=\cos 2\theta\cos\varphi,\quad T_{1c,1s}=-\cos 2\theta\sin\varphi\ ,$$

$$T_{1c,2c}=-\tfrac{1}{2}\sin 2\theta\cos 2\varphi,\quad T_{1c,2s}=\tfrac{1}{2}\sin 2\theta\sin 2\varphi\ ,$$

$$T_{1s,0}=0,\quad T_{1s,1c}=\cos\theta\sin\varphi,\quad T_{1s,1s}=\cos\theta\cos\varphi\ ,$$

$$T_{1s,2c}=-\sin\theta\sin 2\varphi,\quad T_{1s,2s}=-\sin\theta\cos 2\varphi\ ,$$

$$T_{2c,0}=\frac{\sqrt{3}}{2}\sin^2\theta,\quad T_{2c,1c}=\tfrac{1}{2}\sin 2\theta\cos\varphi,\quad T_{2c,1s}=-\tfrac{1}{2}\sin 2\theta\sin\varphi\ ,$$

$$T_{2c,2c}=\tfrac{1}{2}(1+\cos^2\theta)\cos 2\varphi,\quad T_{2c,2s}=-\tfrac{1}{2}(1+\cos^2\theta)\sin 2\varphi\ ,$$

$$T_{2s,0}=0,\quad T_{2s,1c}=\sin\theta\sin\varphi,\quad T_{2s,1s}=\sin\theta\cos\varphi\ ,$$

$$T_{2s,2c}=\cos\theta\sin 2\varphi,\quad T_{2s,2s}=\cos\theta\cos 2\varphi\ .$$

APPENDIX D: MAXIMUM SIGNAL-TO-NOISE RATIO

Consider a set of N data

$$y_i=s_i+n_i,\quad i=1,2,\ldots,N\ , \tag{D1}$$

where s_i is a known signal, and n_i is a random variable with zero mean and variance σ_i^2. The random variables are assumed to be uncorrelated.

We manipulate the data y_i with a linear filter, i.e., form a linear combination of y_i with weight coefficients L_i,

$$Z=\sum_{i=1}^{N}L_iy_i\ . \tag{D2}$$

Z consists of two parts, one associated with the signal s_i,

$$Z_s=\sum_{i=1}^{N}L_is_i\ , \tag{D3}$$

and the other corresponding to the noise n_i,

$$Z_n=\sum_{i=1}^{N}L_in_i\ . \tag{D4}$$

At the filter's output, the signal energy is

$$E_S=Z_s^2=\left(\sum_{i=1}^{N}L_is_i\right)^2\ , \tag{D5}$$

and the noise power is

$$\begin{aligned}E_N&=E\{Z_n^2\}\\&=E\left\{\sum_{i=1}^{N}\sum_{j=1}^{N}L_iL_jn_in_j\right\}\\&=\sum_{i=1}^{N}\sum_{j=1}^{N}L_iL_jE\{n_in_j\}\\&=\sum_{i=1}^{N}L_i^2\sigma_i^2\ ,\end{aligned} \tag{D6}$$

where $E\{\cdots\}$ denotes the ensemble average. The last equality in Eq. (D6) is obtained because the noise is uncorrelated,

$$E\{n_in_j\}=\sigma_i^2\delta_{ij}\ . \tag{D7}$$

The signal-to-noise ratio is therefore

$$\frac{S}{N} = \frac{E_S}{E_N} = \frac{\left(\sum_{i=1}^{N} L_i s_i\right)^2}{\sum_{i=1}^{N} L_i^2 \sigma_i^2} \leq \sum_{i=1}^{N} \frac{s_i^2}{\sigma_i^2} . \quad \text{(D8)}$$

The last inequality follows from the Schwartz inequality. The equality occurs when

$$L_i = c\frac{s_i}{\sigma_i} , \quad \text{(D9)}$$

where c is a nonzero arbitrary constant. L_i in Eq. (D9) is the optimal linear filter that maximizes the signal-to-noise ratio. The maximum signal-to-noise ratio is then

$$S/N = \sum_{i=1}^{N} \frac{s_i^2}{\sigma_i^2} . \quad \text{(D10)}$$

[1] R. L. Forward, Gen. Relativ. Gravit. **2**, 149 (1971).
[2] R. V. Wagoner and H. J. Paik, in *Gravitazione Sperimentale* (Academia Nazionale dei Lincei, Rome, 1977).
[3] W. W. Johnson and S. M. Merkowitz, Phys. Rev. Lett. **70**, 2367 (1993).
[4] M. Cerdonio *et al.*, Phys. Rev. Lett. **71**, 4107 (1993).
[5] Z. Zhou, Ph.D. thesis, Stanford University, 1994.
[6] S. V. Dhurandhar and M. Tinto, Mon. Not. R. Astron. Soc. **234**, 663 (1988).
[7] M. Tinto and S. Dhurandhar, Mon. Not. R. Astron. Soc. **236**, 621 (1989).
[8] Y. Gürsel and M. Tinto, Phys. Rev. D **40**, 3884 (1989).
[9] A. E. H. Love, *A Treatise of the Mathematical Theory of Elasticity* (Dover, New York, 1944).
[10] G. W. Misner, K. S. Thorne, and J. A. Wheeler, *Gravitation* (Freeman, New York, 1973).
[11] B. F. Schutz, *A First Course in General Relativity* (Cambridge University Press, Cambridge, England, 1985).
[12] N. Ashby and J. Dreitlein, Phys. Rev. D **12**, 336 (1975).
[13] S. P. Boughn *et al.*, Astrophys. J. **261**, L19 (1982).
[14] J. Chiang, P. Michelson, and J. Price, Nucl. Instrum. Methods Phys. Res. Sect. A **311**, 603 (1992).
[15] E. Hu, C. Zhou, L. Mann, P. Michelson, and J. Price, Phys. Lett. A **157**, 209 (1991).
[16] P. F. Michelson *et al.*, in *Gravitational Astronomy: Instrument Design and Astrophysical Prospects*, edited by D. E. McClelland and H.-A. Bachor (World Scientific, Singapore, 1991).
[17] N. Solomonson, W. O. Hamilton, W. Johnson, and B. Xu, Rev. Sci. Instrum. **65**, 174 (1994).
[18] T. R. Stevenson, Ph.D. thesis, Stanford University, 1991.
[19] H. J. Paik, Ph.D. thesis, Stanford University, 1974.
[20] P. F. Michelson and R. C. Taber, Phys. Rev. D **29**, 2149 (1984).
[21] J. Price, Phys. Rev. D **36**, 3555 (1987).
[22] P. F. Michelson and R. C. Taber, J. Appl. Phys. **52**, 4313 (1981).
[23] D. M. Eardley, in *Gravitational Radiation*, edited by N. Deruelle and T. Piran (North-Holland, Amsterdam, 1982).
[24] F. B. Estabrook, Gen. Relativ. Gravit. **17**, 719 (1985).
[25] R. L. Forward, Phys. Rev. D **17**, 379 (1978).
[26] B. F. Schutz and M. Tinto, Mon. Not. R. Astron. Soc. **224**, 131 (1987).
[27] A. R. Edmonds, *Angular Momentum in Quantum Mechanics* (Princeton University Press, Princeton, 1957).
[28] A. D. Whalen, *Detection of Signals in Noise* (Academic, New York, 1971).
[29] M. Mohanty, *Signal Processing* (Van Nostrand–Reinhold, New York, 1987).
[30] A. Abramovici *et al.*, Science **26**, 325 (1992).
[31] E. Amaldi *et al.*, Astron. Astrophys. **216**, 325 (1989).
[32] K. S. Thorne, in *300 Years of Gravitation*, edited by S. W. Hawking and W. Israel (Cambridge University Press, Cambridge, England, 1987).
[33] G. A. Tammann, in *Supernovae: A Survey of Current Research*, edited by M. J. Rees and R. J. Stoneham (Reidel, Dordrecht, 1981).
[34] D. G. Blair, in *Gravitational Radiation*, edited by N. Deruelle and T. Piran (North-Holland, Amsterdam, 1983).
[35] C. Cutler *et al.*, Phys. Rev. Lett. **70**, 2984 (1993).
[36] B. F. Schutz, in *The Detection of Gravitational Waves*, edited by D. G. Blair (Cambridge University Press, Cambridge, England, 1991).
[37] R. Narayan, T. Piran, and A. Shemi, Astrophys. J. **379**, L17 (1991).
[38] E. S. Phinney, Astrophys. J. **380**, L17 (1991).
[39] R. A. Hulse and J. H. Taylor, Astrophys. J. **368**, 504 (1975).
[40] G. H. Stokes, J. H. Taylor, and R. J. Dewey, Astrophys. J. **294**, L21 (1985).
[41] S. B. Anderson *et al.*, Nature (London) **346**, 42 (1990).
[42] A. Wolszczan, Nature (London) **350**, 688 (1991).